Draft Manuscript for Review

Rhyolite generation prior to a Yellowstone supereruption: Insights from the Island Park-Mount Jackson rhyolite series

Journal:	*Journal of Petrology*
Manuscript ID	JPET-Oct-15-0118.R2
Manuscript Type:	Original Manuscript
Date Submitted by the Author:	n/a
Complete List of Authors:	Troch, Juliana; Institute of Geochemistry and Petrology, ETH Zurich Ellis, Ben; ETH, Geochemistry and Petrology Mark, Darren; Argon Isotope Facility, Scottish Universities Environmental Research Centre (SUERC) Bindeman, Ilya; University of Oregon, Geological Sciences Kent, Adam; Oregon State University, College of Earth, Ocean and Atmospheric Sciences Guillong, Marcel; Institute of Geochemistry and Petrology, ETH Zurich Bachmann, Olivier; Eidgenössische Technische Hochschule, Department of Earth sciences, Institute of Geochemistry and Petrology
Keyword:	Yellowstone, rhyolite, crystal fractionation, recycling, petrogenesis

Rhyolite generation prior to a Yellowstone supereruption: Insights from the Island Park-Mount Jackson rhyolite series

[1]Juliana Troch*, [1]Ben S. Ellis, [2]Darren F. Mark, [3]Ilya N. Bindeman, [4]Adam J.R. Kent, [1]Marcel Guillong, [1]Olivier Bachmann

[1]Institute for Geochemistry and Petrology, ETH Zurich, Clausiusstrasse 25, 8092 Zurich, Switzerland,

[2]Argon Isotope Facility, Scottish Universities Environmental Research Centre (SUERC), Rankine Avenue, East Kilbride, G75 0QF, Scotland

[3]Department of Geological Sciences, University of Oregon, Eugene, OR 97403, USA

[4]College of Earth, Ocean, and Atmospheric Sciences, 104 Ocean Admin, Oregon State University, Corvallis, OR 97330, USA

* Corresponding author: juliana.troch@erdw.ethz.ch, Tel: (+41) 44 633 81 04

ABSTRACT

The Yellowstone volcanic field is one of the largest and best-studied centres of rhyolitic volcanism on Earth, yet it still contains little-studied periods of activity. Such an example is the Island Park-Mount Jackson series, which erupted between the Mesa Falls and Lava Creek caldera-forming events as a series of rhyolitic domes and lavas. Here we present the first detailed characterisation of these lavas and use our findings to provide a framework for rhyolite generation in Yellowstone between 1.3 and 0.6 Ma, as well as to assess whether magmatic evolution hints at the forthcoming super eruption.

These porphyritic (15-40% crystals) lavas contain mostly sanidine and quartz with lesser amounts of plagioclase (consistent with equilibrium magmatic modelling via rhyolite-MELTS) and a complex assemblage of mafic minerals. Mineral compositions vary significantly between crystals in each unit, with larger ranges than expected from a single homogeneous population in equilibrium with its host melt. Oxygen isotopes in quartz and sanidine indicate slight depletions ($\delta^{18}O_{magma}$ of 5.0-6.1‰), suggesting some contribution of localised remelting of hydrothermally altered material in the area of the previous Mesa Falls Tuff-related caldera collapse. The preservation of variable O isotopic compositions in quartz requires crystal entrainment less than a few thousand years prior to eruption. Late entrainment of rhyolitic material is supported by the occurrence of subtly older sanidines observable in single-grain $^{40}Ar/^{39}Ar$ geochronology. Eruption ages of the lavas show discrete clusters illustrating that extended quiescence (>100 ka) in magmatic activity may be a re-occurring feature in Yellowstone volcanism.

Ubiquitous crystal aggregates dominated by plagioclase, pyroxene and Fe-Ti oxides are interpreted as cumulates co-erupted with their extracted liquid. Identical crystal aggregates are found in both normal-$\delta^{18}O$ and low-$\delta^{18}O$ rocks from Yellowstone, indicating that common

petrogenetic processes characterise both volcanic suites, including the late-stage extraction of melt from an incrementally-built upper crustal mush zone.

Keywords: *Yellowstone, rhyolite, ~~super eruption~~petrogenesis, crystal fractionation, recycling*

INTRODUCTION

The largest silicic eruptions on Earth are produced from caldera-forming explosive volcanism. While events on the scale of the 5 km^3 eruption of Pinatubo in 1991 can result in measurable global climatic effect (Minnis *et al.*, 1993), the geological record illustrates that the largest silicic eruptions can be as much as three orders of magnitude larger (Self, 2006, Hildreth & Wilson, 2007). The catastrophic consequences emphasise the importance of a detailed scientific investigation of the mechanisms controlling the generation of these large volumes of rhyolitic magma that can culminate in so-called super eruptions.

At large, long-lived caldera centres such as Yellowstone, the catastrophic explosive events represent only a tiny fraction of the lifespan of the volcanic centre; the majority of ~~time~~ activity is taken up by relatively quiescent effusion of lava and intermittent minor explosive activity. Studying this effusive activity preceding and post-dating large-volume eruptions is key to understanding the magmatic system as a whole, and can be addressed over shorter timescales via geophysical methods (Chang *et al.*, 2007) and over longer timescales via assessment of the compositional evolution of the reservoir (Vazquez *et al.*, 2009). Such an assessment includes questions of how such huge volumes of magma are generated, stored in the crust and erupted, with a particular focus on the processes and temporal relations in the generation of these magmas.

The formation of rhyolites in the Yellowstone province remains a topic of active debate with two proposed end-member models: (1) a fractionation-dominated evolution with subordinate

assimilation in an upper crustal mush zone (Vazquez & Reid, 2002, Vazquez *et al.*, 2009, Girard & Stix, 2010, Stelten *et al.*, 2015) and (2) bulk or partial crustal melting initiated by intrusion of basaltic and/or silicic magma as a heat source with limited mass contribution (Bindeman & Valley, 2001, Bindeman *et al.*, 2008, Simakin & Bindeman, 2012). While the first model is mainly based on mineralogical and geochronological studies of young Yellowstone lavas, the second scenario has received significant support from oxygen isotope studies. These revealed rhyolitic lavas with unusual $\delta^{18}O$ characteristics and isotopically diverse phenocrysts, suggesting melting of hydrothermally altered lithologies in the shallow crust. In this study, we evaluate the applicability of these models to the record of lavas erupted prior to Yellowstone's latest super eruption at 0.631 Ma (Matthews *et al.*, 2015). The Island Park-Mount Jackson rhyolite series represents a prime example of a series of effusive events that preceded an explosive eruption, but has yet received little attention. By coupling major and trace elements in whole rock, glasses and minerals to oxygen and Pb isotopic data and $^{40}Ar/^{39}Ar$-ages, we obtain a detailed petrological and geochemical characterisation of these lavas to provide a framework for rhyolite generation in Yellowstone and to test whether the mineralogical and geochemical records were hinting at the forthcoming super eruption.

GEOLOGICAL BACKGROUND

The Yellowstone volcanic field represents the current focus of volcanism, which has been ongoing for at least 16.5 Ma covering vast areas of the Northwest of the USA. The Columbia River-Snake River Plain-Yellowstone province is compositionally bimodal (basalt-rhyolite) and most commonly interpreted as the result of a hotspot (Geist & Richards, 1993, Hooper *et al.*, 2007, Wolff *et al.*, 2008). Silicic volcanism in the province was initially widely dispersed (e.g. Coble & Mahood, 2012), prior to becoming focused along the track of the Snake River Plain from around 14 Ma. Here, numerous voluminous ignimbrites and lavas were produced,

with more frequent explosive eruptions and higher magmatic temperatures compared to the younger part of the province (Cathey & Nash, 2009, Ellis *et al.*, 2013).

Silicic volcanism at Yellowstone has been ongoing for the past 2 Ma and is characterised by large-volume explosive eruptions separated by periods of relative quiescence during which effusion of rhyolitic lava dominates (Christiansen, 1984, Christiansen, 2001). The explosive eruptions consist of the Huckleberry Ridge Tuff (HRT) at 2.1 Ma (Rivera *et al.*, 2014b), the Mesa Falls Tuff (MFT) at 1.3 Ma (Lanphere *et al.*, 2002), and the Lava Creek Tuff (LCT) at 0.6 Ma (Lanphere *et al.*, 2002, Matthews *et al.*, 2015, Wotzlaw *et al.*, 2015). These voluminous deposits provide regionally significant stratigraphic markers and separate Yellowstone volcanism into three volcanic cycles (Christiansen, 2001).

Following the early studies which considered Yellowstone volcanism as a whole (e.g. Christiansen & Blank, 1972, Doe *et al.*, 1982, Hildreth *et al.*, 1984, Hildreth *et al.*, 1991, Christiansen, 2001), more recent work has focused separately on the large explosive events and the youngest volcanism after the LCT, namely the Upper Basin Member and Central Plateau Member (e.g. Obradovich, 1992, Gansecki *et al.*, 1996, Bindeman & Valley, 2001, Lanphere *et al.*, 2002, Vazquez & Reid, 2002, Bindeman *et al.*, 2008, Girard & Stix, 2009, Vazquez *et al.*, 2009, Girard & Stix, 2010, Ellis *et al.*, 2012, Watts *et al.*, 2012). To improve the understanding of the early history of Yellowstone, we investigate the ~~poorly known~~less-documented Island Park domes and Mount Jackson lavas, which were erupted between the MFT and the LCT, thus spanning the second and third volcanic cycle in Yellowstone (Christiansen, 2001).

The Island Park – Mount Jackson (IPMJ) rhyolite series

The Island Park (IP) domes include the undated units Silver Lake dome, Lookout Butte and Elk Butte, as well as Osbourne Butte (1.28±0.01 Ma) and Warm River Butte (1.24±0.02 Ma,

all K/Ar ages by Obradovich, 1992). These domes are located in a NW-SE trending zone inferred to be tectonically controlled (Christiansen, 2001), with only the Lookout Butte dome erupted along what is thought to be the caldera related to the MFT (Fig. 1). Historically, the notably small-volume IP domes are thought to represent post-caldera units relating to the preceding MFT-related caldera collapse, whereas the volumetrically larger Mount Jackson (MJ) rhyolite lava flows are interpreted as pre-caldera units of the following LCT eruption (Christiansen, 2001). Units from the MJ series are widely dispersed across the Yellowstone volcanic field and include the Moose Creek flow (1.22±0.01 Ma), Wapiti Lake flow (1.16±0.01 Ma), Flat Mountain Rhyolite (0.929±0.034 Ma), Lewis Canyon Rhyolite (0.853±0.007 Ma), Harlequin Lake flow (0.839±0.008 Ma), Big Bear Lake flow (undated) and Mount Haynes Rhyolite (0.609±0.006 Ma, all K/Ar ages by Obradovich, 1992). These lava flows were proposed to be tracing an arcuate fault structure, which was later exploited during the LCT eruption (Christiansen, 2007). Although the origin of such an arcuate structure prior to caldera collapse remains unclear, it could have been the result of piecemeal caldera-related faulting during the eruption of the earlier HRT. Notably, the MJ rhyolites are morphologically similar to the voluminous rhyolite lavas of the Plateau Member, whereas rhyolites from the IP series are much smaller and have dome-like structures (Fig. 1). Within the MJ lavas lies the Lewis Canyon Rhyolite which is inferred to represent an unknown number of lavas which are petrologically dissimilar to the other MJ lavas in containing significantly more plagioclase (Christiansen & Blank, 1972, Christiansen, 2001). We therefore mention this unit separately in the results and discussion sections.

METHODS

Major and trace element analyses

Samples were analysed for bulk geochemistry via XRF and ICP at the GeoAnalytical Laboratory at Washington State University following the procedures described in Johnson *et al.* (1999). For mineral separates, rocks were fragmented using a SELFRAG at ETH Zurich. Following cleaning, samples were separated further if necessary via heavy liquid separation and minerals picked by hand under a binocular microscope.

Electron microprobe analyses of mafic minerals were performed at the University of Kiel (Germany) with a JXA 8900 R Electron Microanalyser. 20-30 grains per unit were measured for rim and core composition. Fayalite was analysed with 20 keV and 15 nA, pyroxene and hornblende with 15 keV and 15 nA. Standard measurements for all EMP and LA ICP MS analyses can be found in the electronic supplementary material.

Cathodoluminescence images of 25-30 epoxy-mounted quartz grains per sample were obtained at the Scientific Centre for Optical and Electron Microscopy (ScopeM) at ETH Zurich on a FEI Quanta 200 scanning electron microscope. Individual grains were evaluated for zonation grade (strongly zoned, gradual changes or unzoned) and direction (unidirectional bright core-dark rim or dark core-bright rim? Oscillatory zoning?). In the same fashion, sanidine grains from five representative units (IP units Osbourne Butte and Silver Lake dome, MJ units Moose Creek flow, Lewis Canyon Rhyolite and Mt. Haynes Rhyolite) were imaged for CL prior to trace element analysis.

Analyses on feldspars were performed at ETH Zurich with a Jeol JXA 8200 electron microprobe at 15 keV and 15 nA. On all grains a minimum of two points were measured to obtain rim and core compositions. Beam diameter was set to 10 µm and counting times were shortened for Na and K to avoid element mobility. Glass shards were analysed with a beam of 20 µm and 12 nA at 15 kV.

A 193nm Resonetics Resolution 155 excimer laser ablation system coupled to a Thermo Element XR sector field mass spectrometer was used to determine trace element in quartz,

feldspar and glass at ETH Zurich. Spot sizes were 43 or 67 microns and samples were ablated using 5 Hz for 40 seconds after 30 s of gas blank acquisition. NIST 612 was used as a primary standard and GSD-1G as a secondary standard for quality control. Data was reduced using SILLS software (Guillong *et al.*, 2008) with SiO_2 contents from previous EMP analyses used as internal standard (or taken as 100% for quartz). Trace element determinations are considered to be precise and accurate within 5% of the reported values based on long-term reproducibility of a variety of glass standards.

^{40}Ar/^{39}Ar dating

For ^{40}Ar/^{39}Ar geochronology, sanidine separates were handpicked under a binocular microscope from the 0.5 to 1 mm size fraction with care taken to avoid inclusions of glass or minerals and visible alteration. Samples were tested with the method of Hynek *et al.* (2011) to ensure a pure sanidine separate, before being cleaned and packed for irradiation at the CLICIT facility of the OSU reactor. 16-31 crystals per unit were placed into high-purity Al irradiation disks with samples of Alder Creek (ACs, age 1.2056 Ma) and Fish Canyon sanidine (FCs-EK, age 28.294 Ma, Morgan *et al.*, 2014). Most samples were irradiated for 1 hour in June 2013, but were not run due to laboratory issues. They were re-irradiated (along with the same monitors) for 1 hour in November 2014 and analysed in January 2015. Wapiti Lake was irradiated for 2 hours in October 2014 and analysed in January 2015 (note this sample was not a re-irradiation). Following irradiation and cooling, sanidine samples were fused using a CO_2 laser. Extracted gases were subjected to 300 s of purification by exposure to two SAES GP50 getters at room temperature and at 450˚C (for full system technical details see Mark *et al.*, 2012). Isotope measurements were made using a MAP 215-50 noble gas spectrometer.

All Ar isotope data were corrected for backgrounds (average ± standard deviation from entire run sequence), mass discrimination (calculated from air calibration shots of 7.32 x 10^{-14} moles ^{40}Ar), and reactor-produced nuclides, before being processed using standard data reduction protocols (Mark *et al.*, 2005) and reported according to the criteria of Renne *et al.* (2009) and relative to the optimisation model of Renne *et al.* (2010, 2011). We employed the atmospheric argon isotope ratios of Lee *et al.* (2006), which have been independently verified by Mark *et al.* (2011) and are consistent with inverse isochron plots for individual units. The eruption age of each unit is calculated from the weighted means of eruption-age total fusion ages of individual sanidines ~~Ages were calculated relative to the optimisation model of Renne *et al.* (2010, 2011)~~ and is~~are~~ reported as X ± Y/Z (2 sigma confidence level), where Y is the analytical uncertainty and Z is the full external precision, including uncertainty from the decay constant.

Isotopic analyses

Lead isotope compositions in sanidine crystals were measured using laser ablation multicollector inductively-couple plasma mass spectrometry (LA-MC-ICP-MS), with a Photon Machines G2 excimer laser ablation system and NuPlasma MC-ICP-MS at Oregon State University. Analytical techniques follow those given in Kent (2008). Analyses were made using a single 85 µm laser spot translated at 5 µm/sec and a pulse frequency of 7 Hz on each grain. Measured ratios were corrected for mass bias based on measurement of NIST-612 standard glass at similar ablation conditions throughout the analysis session. Repeated analysis on standard reference BCR-2G glasses were typically within 0.01-0.22% of the accepted values.

Quartz and sanidine separates for O isotopic determinations were cleaned using dilute HNO_3 to remove any trace of adhering groundmass. Aliquots of 1-2 mg (typically 2-4 grains) were

then analysed by CO_2-laser fluorination at the University of Oregon using BrF5 as reagent, an Hg diffusion pump fluorine getter and a MAT253 mass spectrometer (Bindeman *et al.*, 2008). The long term reproducibility of standards is ±0.07‰ (1 stdev) during runs where standards are run concurrently with the unknowns and of ±0.2‰ (1 stdev) during airlock runs where samples are run one by one.

RESULTS

Sample description

Samples were collected of the rhyolitic domes of the Island Park series (Osbourne Butte, Lookout Butte, Warm River Butte, Elk Butte and Silver Lake dome), as well as of the rhyolitic lava flows of the Mount Jackson Member (Moose Creek flow, Wapiti Lake flow, Harlequin Lake flow and Mt. Haynes flow), and the Lewis Canyon Rhyolite. The groundmass in the IPMJ rhyolites is microcrystalline, often displaying spherulitic textures and flow banding. The IP units Silver Lake dome, Osbourne Butte, Elk Butte and Lookout Butte are only partially devitrified and still contain some glass. IPMJ rhyolites are porphyritic with the IP rhyolites being more crystal-rich (28-39%) than the MJ rhyolites (13-19%). The mineral assemblage consists of ~6-26% sanidine, ~4-17% quartz, ~2-7% plagioclase, and ~1-3% Fe-Ti oxides and mafic minerals, such as clinopyroxene, orthopyroxene, amphibole and fayalite (table 1). Biotite, zircon and allanite occur as accessory phases. Magnetite and ilmenite are usually exsolved. Some units (Warm River Butte and Lookout Butte) contain blebs with myrmekitic intergrowth of K-feldspar and quartz. The Lewis Canyon Rhyolite is petrographically distinct and shows abundant plagioclase (~7%) with a concurrent decrease in the amount of sanidine and quartz.

Bulk and glass compositions

All IPMJ samples are rhyolitic in composition with the majority being high-silica (>75 wt% SiO_2 on anhydrous basis) rhyolites (table 2), except for Osbourne Butte and Lookout Butte (74.0 and 73.5 wt% SiO_2 respectively). Like most Yellowstone rhyolites, the IPMJ rhyolites are relatively potassic with K_2O and Na_2O typically ranging around 5.2 wt% and 3.3 wt% respectively.

Only the IP domes and the Wapiti Lake flow contain glass ~~that can be analysed~~, in all other flows the groundmass is microcrystalline. Glass contains ~76-78 wt% SiO_2 (recalculated anhydrous) in the IP domes and ~78 wt% SiO_2 in the Wapiti Lake flow with original totals of ~96-99 wt% (Supplement). Glass shards contain high amounts of Rb (100-640 ppm) and Zr (120-160 ppm) and notably low contents of Sr (<10 ppm) and Eu. REE patterns of the glasses mimic those of the bulk samples with both MJ and IP rhyolites exhibiting 'seagull-shaped' REE patterns with a deep negative Eu anomaly and relatively straight high concentrations in LREE and HREE (Fig. 2). These signatures are typical for rhyolites from the Snake River Plain-Yellowstone volcanic suite (Ellis *et al.*, 2013) and characteristic for hot and dry volcanic settings (Bachmann & Bergantz, 2008).

$^{40}Ar/^{39}Ar$ geochronology

Single crystal $^{40}Ar/^{39}Ar$ ages for the IPMJ series range between 1.2943±0.0020/0.0026 and 1.2190±0.0144/0.0146 Ma for the IP domes and between 1.2856±0.0064/0.0066 and 0.7016±0.0014/0.0016 Ma for the MJ rhyolites, thus both series overlap by 0.066 Ma. All ages with their respective uncertainties are presented in table 3. Contrary to conclusions from Christiansen (2001) based on field observations and preliminary K-Ar dates on some of the units, there is no time gap between the IP domes and the MJ rhyolite series and both the Moose Creek flow (1.2856±0.0064/0.0066 Ma) and the Wapiti Lake flow (1.2187±0.0158/0.0160 Ma) overlap with ages from the IP domes. However, there is a

significant time gap between the eruption of Wapiti Lake flow at 1.2187±0.0156/0.0160 Ma and the eruption of the subsequent Flat Mountain Rhyolite at 0.93 Ma (K-Ar age from Obradovich (1992), not sampled in this study). Among the MJ rhyolites, the Moose Creek flow is the oldest and erupted close to the MFT-related Henry Forks caldera (Fig. 3). The MJ-rhyolite Wapiti Lake flow erupted contemporaneously with the last of the IP domes, but at the ~~northeastern~~north-eastern end of the volcanic field. Coherent with observations from other Yellowstone rhyolites (Gansecki *et al.*, 1996, Gansecki *et al.*, 1998, Lanphere *et al.*, 2002, Dallegge, 2008, Ellis *et al.*, 2012, Rivera *et al.*, 2014b, Stelten *et al.*, 2015), many of the IP and MJ lavas show subtly older sanidine grains, which are too old to be part of the eruption-age population (Fig. 3). It cannot be entirely excluded that apparent "too-old" $^{40}Ar/^{39}Ar$ ages were caused by excess Ar hosted in minute melt or fluid inclusions, however, we note that all dated grains were screened for inclusions under a binocular microscope.

Quartz

Quartz is a ubiquitous mineral phase in all IPMJ rhyolites. Crystals are commonly subhedral, rounded in shape and ~1.5-2 mm in diameter, but reach up to 3 mm in the Warm River Butte. Quartz crystals commonly host melt inclusions with sizes from ~10-200 µm. CL imaging reveals a lack of systematic zonation (i.e. same zonation pattern in majority of crystals) with most of the grains displaying gradual transitions between several generations of dark and bright zones (Fig. 4). Within a unit, several modes of zonation are observed, from non-zoned grains to a few that are strongly zoned. Quartz grains in most of the units feature darker rims whereas a few grains from the Lewis Canyon (~15%) and the Silver Lake dome (~14%) show an abrupt late change to bright rims. Minor discordant growth zones indicate periods of resorption followed by new crystallisation. No correlations were observed with changes in crystal sizes.

Ti contents correlate with ~~trace element~~ contents of Al (73-130 ppm) and Li (15-28 ppm) and are in good agreement with relative CL brightness distributions (Fig. 4), consistent with them being the main control of CL brightness (e.g. Leeman *et al.*, 2012 and references therein). Quartz grains feature a wide range of Ti contents (35-206 ppm), similar to those observed in post-LCT rocks (e.g. Vazquez *et al.*, 2009, Girard & Stix, 2010, Leeman *et al.*, 2012). Different crystals in the same unit can be zoned from lower to higher Ti values from core to rim, from higher to lower Ti values, or show no zonation at all, thus do not record a systematic compositional evolution with time. In most units, the Ti contents in rims of different grains are relatively similar even when different crystals display a variable intra-grain Ti-evolution. All trace elemental data for quartz and details regarding CL brightness and zonation of grains are provided in the supplementary materials.

Feldspars

The IPMJ rhyolites contain both sanidine and plagioclase. However, the two phases occur in markedly different contexts: Sanidine is the dominant feldspar within all IPMJ rhyolites except for the Lewis Canyon Rhyolite, occurring as euhedral, single crystals showing scant optical zonation and rarely containing melt inclusions. Sizes range from ~0.6 to 2.5 mm in diameter with the largest sizes occurring in the Warm River Butte, yet even the largest sanidines observed are smaller than the cm-sized sanidines in the MFT (Christiansen, 2001). By contrast, plagioclase is relatively rare in the IPMJ rhyolites with the exception of the Lewis Canyon Rhyolite. Crystal sizes range from 0.2 to 2 mm, commonly displaying small melt inclusions. A few crystals have sieve textures, a feature that has been previously described for the post-LCT lavas (Hildreth *et al.*, 1984, Girard & Stix, 2009, Watts *et al.*, 2012) and can be overgrown by sanidine. Optical zonation is rare and seemingly limited to very large crystals (>0.8 mm). Plagioclase is most commonly found within polymineralic

glomerocrysts *(see later)*, which are dominated by pyroxene, plagioclase and Fe-Ti oxides and may contain accessory zircon and apatite with some interstitial groundmass.

Compositionally, all sanidines from the IPMJ series are similar and range from Or_{43} to Or_{63}, with the end member compositions from the Lewis Canyon (Or_{43-55}) and the Moose Creek (Or_{59-63}) samples. Intra-grain major elemental compositional variability is limited, typically less than Or_{1-2}. Plagioclase features compositions between An_{11-36}, with end members being the Mt. Haynes Rhyolite (An_{11-22}) and the Warm River Butte (An_{21-36}). Generally, plagioclase from the IP rhyolites shows slightly higher An-contents compared to MJ lavas (Fig. 5). Both IPMJ sanidine and plagioclase resemble previously reported compositions in Yellowstone rhyolites (Hildreth *et al.*, 1984, Gansecki *et al.*, 1996, Girard & Stix, 2009, 2010, Stelten *et al.*, 2015).

Trace elemental data from sanidines does not distinguish the different units with the exception of sanidine from the Lewis Canyon Rhyolite, which contains more Sr and Ba. Rather, sanidines within each of the IPMJ rhyolites are characterised by large spreads in trace elemental compositions between different grains, often equally as large as the range of trace element contents within sanidines from the entire IPMJ series. CL imaging of sanidines in a subset of rhyolites reveals diverse modes of zonation between different grains similar to observations in quartz. IP sanidines show both oscillatory and unidirectional zoning. Strong reverse, mostly unidirectional zoning with bright CL-rims occurs in MJ rhyolites with strong variations of trace elements such as Ba, Sr, Eu, and Ti between core and rim. Sanidines in the Lewis Canyon rhyolite record Ba contents of up to 10,000 ppm in rims (compared to ~7,500 ppm in cores), to a lesser degree rim-enrichment can also be observed in Sr contents. IP sanidines exhibit larger inter-grain variability and show no preferred direction of zonation in trace element space. Inter-grain variability and possible causes for Ba-enriched sanidine rims are discussed later in more detail.

Mafic minerals

Mafic minerals are generally rare in the IPMJ rhyolites. Previously, these lavas were described as containing clinopyroxene and orthopyroxene in addition to accessory fayalite and Fe-hornblende (Hildreth *et al.*, 1984, Christiansen, 2001). However, in some of the studied lavas, particularly those of the IP series, fayalite and hornblende (Fig. 6) are abundant and reach up to 60% of the mafic mineral assemblage (table 1). Where both pyroxenes are present, clinopyroxene is more abundant. However, there are cases where clinopyroxene (Warm River Butte, Wapiti Lake flow, Harlequin Lake flow) or orthopyroxene (Mt. Haynes Rhyolite) is sufficiently rare to be absent in mineral separates.

Despite limited intra-grain variability, compositional ranges in clinopyroxenes are large between different grains ($En_{11-38}Wo_{30-48}$, Fig. 7). Mg# averages for each unit range from 32±7 to 44±2, whereas individual crystals can reach Mg# of up to 70. The degree of scatter varies markedly between units, e.g. clinopyroxenes from the IP domes Lookout Butte, Osbourne Butte and Silver Lake dome cluster around Mg# = 33±7 with individual grains as high as 56, whereas grains from Lewis Canyon Rhyolite have values of around 45±2. Orthopyroxene has compositions of $En_{18-65}Wo_{02-15}$. Additionally, the Mt. Haynes Rhyolite contains pure ferrosilite with >2 wt% MnO and <0.1 wt% MgO. Both ortho- and clinopyroxenes can often be found in crystal aggregates with plagioclase and iron oxides (see separate discussion); these aggregate-hosted pyroxenes are compositionally identical to single pyroxenes in the groundmass.

The REE abundances in clinopyroxene are similar to patterns observed in whole rock trace elements and show elevated contents in LREE and HREE and a marked Eu anomaly (Fig. 8). Orthopyroxenes show similar behaviour with the majority of grains having LREE > HREE and elevated contents in Zr, Sr and Sc. A minority of both clinopyroxene and orthopyroxene

have LREE < HREE, lower overall abundances of REE, lack a pronounced Eu anomaly and have Mg# > 60.

Fayalite is restricted to the IP domes and the Moose Creek flow. Forsterite contents range from 6 to 15, slightly higher than the 2-7 reported by Vazquez *et al.* (2009) for post-LCT lavas. Fayalites commonly show altered rims and oxidation features involving the transformation to iron oxides and hydroxides along cracks (Fig. 6). In trace elements, the majority of grains show an evolved character with LREE > HREE and marked Eu anomalies, while a minority of crystals have low LREE contents and a less pronounced Eu anomaly (Fig. 8).

Amphiboles are Fe-hornblende with subhedral shapes without zoning or alteration features (Fig. 6). They occur commonly in IP domes, Moose Creek flow and the Lewis Canyon Rhyolite. All hornblendes display pronounced negative Eu anomalies and high contents of LREE and HREE (Fig. 8).

Oxygen isotopes

Oxygen isotopic compositions were determined on quartz and sanidine with ranges of 4.7 to 6.9 ‰ for quartz and 4.5 to 6.0 ‰ for sanidine (all data in supplementary materials). Intra-unit variability is large, reaching 1.3‰ in both quartz and sanidine (Fig. 9). Units with lower oxygen isotopic compositions such as the IP domes display more variability in $\delta^{18}O$. MSWDs of quartz populations are mostly higher than the critical MSWD for the analysed number of samples (Mahon, 1996), suggesting significantly more variation than expected for a single population.

Sanidine $\delta^{18}O$ values are 0.5-1.0 ‰ lower than $\delta^{18}O$ for quartz in the same unit. While such divergence can be expected with equilibrium fractionation of $\Delta^{18}O(Qtz\text{-}Fsp)$ = 0.75 ‰ in silicic magmas at 850±60°C (Bindeman & Valley, 2001), overlaps in $\delta^{18}O$ values between

quartz and sanidine crystals and the large variation of $\delta^{18}O$ within a rhyolite preclude a closed system evolution for the IPMJ rhyolites. Taking average quartz values and assuming a fractionation factor of $\Delta^{18}O$(Qtz-melt) = 0.35 ‰ (Bindeman & Valley, 2001), we estimate magmatic $\delta^{18}O$ values between 4.9 and 6.1 ‰ for different units. Only the youngest MJ lavas are normal-$\delta^{18}O$ rhyolites (defined as 5.8-6.3 ‰, Bindeman, 2008), whereas the majority shows a slight depletion. All units are significantly lower than the $\delta^{18}O$ value of ambient crust (6.8-7.2‰, Fig. 9) or units that show a significant crustal component in oxygen, Pb, Sr and Nd-isotopic space, such as HRT member C and extra-caldera post-LCT rhyolite (Hildreth *et al.*, 1991).

The mildly depleted-$\delta^{18}O$ signature of both the IP and MJ lavas is in good agreement with values previously reported for some of the MJ units (Hildreth *et al.*, 1984, Bindeman & Valley, 2001) with the MJ lavas being slightly higher than the IP domes (Fig. 9). Both the MFT and LCT explosive eruptions have higher $\delta^{18}O$ than the intervening lavas. The pattern of dropping and recovering $\delta^{18}O$ magmatic values following large caldera-forming eruptions is well-documented for Yellowstone (Hildreth *et al.*, 1984, Bindeman & Valley, 2001) with the IPMJ series exhibiting similar behaviour on a smaller isotopic scale. Although inter-crystal O isotopic variability in the IPMJ rhyolites is not as large as in the low-$\delta^{18}O$ post-LCT lavas (Bindeman & Valley, 2001, Watts *et al.*, 2012), it still records a lack of closed-system fractionation throughout the history of Yellowstone.

Pb isotopes

Pb isotopes in sanidine have been proven to be a useful tool for the distinction of units that are very similar in trace element composition (e.g. Watts *et al.*, 2012, Stelten *et al.*, 2015). Data for the IPMJ rhyolites are in the range of previously published data for Yellowstone and differences between units are slight compared to the overall range of Pb isotopes in

Yellowstone (Fig. 10). Values seem to transition from MFT-like to LCT-like compositions with Pb isotopes in the IP domes being close to those of the preceding MFT, whereas MJ units are closer to those of the LCT (Fig. 10). We note that only a single translated spot was analysed per grain and that these analyses were obtained prior to CL imaging and therefore yield no information on whether crystals are zoned in terms of Pb isotopes.

Intensive parameters

Zr-saturation thermometry (Hanchar & Watson, 2003, Boehnke *et al.*, 2013) returns temperatures of 795-858°C for bulk rock compositions with the Lewis Canyon Rhyolite having the highest inferred temperature (table 2). Where glass is present, results for glasses are typically 10-20°C higher than temperatures derived from bulk rock compositions, but within uncertainty. Bulk rock Zr-saturation temperatures from Boehnke *et al.* (2013) are 10-40°C lower than those from Hanchar and Watson (2003) and within error of results from alkali feldspar-liquid thermometry (Putirka, 2008), except for Warm River Butte which returns slightly lower temperatures (771±23°C instead of 814±17°C). All details and input parameters for thermometry calculations can be found in the supplementary material.

Ti-in-quartz thermometry (TitaniQ, Wark & Watson, 2006) was not performed because we were unable to sufficiently constrain a_{TiO2}. Fe-Ti oxides in these lavas are exsolved, therefore prohibiting calculation of a_{TiO2} from co-existing mineral pairs. Given the compositional range of quartz grains in these lavas, magmatic conditions with similar a_{TiO2} in space and time seem unlikely and previously employed activities range from 0.33 to 0.56 between different post-LCT lava flows (Vazquez *et al.*, 2009). Ti activities may change as a function of Ti content in the melt and its major element composition, co-crystallising Fe-Ti oxide composition, oxygen fugacity, and temperature and pressure conditions (e.g. Thomas & Watson, 2012 and references therein). Thus, ~~it~~ a_{TiO2} may have changed significantly throughout the growth

history of even a single quartz grain, suggesting that an averaged a_{TiO2} calculated from co-existing Fe-Ti oxides or TiO_2 solubility models provides only estimates at best.

The previously unrecognised occurrence of abundant amphibole and accessory biotite in the IPMJ rhyolites suggests sufficient presence of water to create hydrous mineral phases (e.g. >4.5 wt% H_2O for formation of amphibole and >2.5 wt% H_2O for biotite in experiments on Yellowstone hotspot track rhyolites by Almeev *et al.* (2012)). Estimates of water contents from plagioclase-melt hygrometers (Putirka, 2008) indicate that about 3.6±1.1 to 5.7±1.1 wt% –H_2O were present during the formation of the IPMJ rhyolites (see supplementary material). Although strongly depending on inferred temperatures, these values are consistent with the generally increasing water contents from the central Snake River Plain to Yellowstone (Almeev *et al.*, 2012, Bolte *et al.*, 2015).

DISCUSSION

Time-space evolution of the Yellowstone volcanic field at 1.3-0.6 Ma

The new $^{40}Ar/^{39}Ar$-geochronology provides insights into the development of the volcanic field during the period between MFT and LCT eruptions. Broadly speaking, volcanism migrated from west to east: Post-caldera activity first focused on the area of the foregone MFT-related caldera collapse with the eruption of the IP domes and the Moose Creek flow, before transitioning to areas surrounding the younger LCT-related caldera, where activity is characterised by eruptions from widely separated regions.

The overlap between the two magmatic series questions the traditional inference of two different cycles with the IP domes marking post-caldera activity of the MFT-forming eruption (2^{nd} cycle) while the MJ succession records pre-caldera activity of the third cycle encompassing the eruption of the LCT (Christiansen, 2001). Both in terms of age and geochemical behaviour the Moose Creek flow is similar to the IP-domes, e.g. in mafic

mineral abundances (table 1), feldspar and pyroxene major and trace element compositions (Figs. 4, 5) and oxygen and Pb isotopic compositions (Figs. 9, 10). Geochemistry may thus largely be controlled by geographical location and source region rather than affiliation with a magmatic series defined by morphology.

The temporal overlap between the MJ and IP series suggests that the different morphologies of IP domes compared to the lava flows of the MJ series are not controlled by a time-progressive evolution. IPMJ volcanism occurred in unevenly distributed clusters of 2-4 lava flows (Fig. 3), coherent with discrete periods of activity observed in the post-LCT record (Christiansen, 2001, Christiansen, 2007). Notably, in some cases lava flows erupted contemporaneously within uncertainty with other flows at the opposite edge of the volcanic field (e.g. Lookout Butte/Wapiti Lake flow), suggesting that batches of broadly similar, yet isotopically subtly distinct liquids were present simultaneously within the crust.

The largest time gap in the IPMJ record is the 290 ka of quiescence starting ~120 ka after the MFT-eruption between the eruptions of Wapiti Lake flow and the Flat Mountain Rhyolite. The post-LCT record equally contains periods of prolonged quiescence, such as the ~180 ka quiescence between the Dunraven Road flow and the following South Biscuit Basin flow (Christiansen, 2007, Bindeman *et al.*, 2008). This similarity suggests that prolonged quiescence (>100 ka) could be a common feature in the effusive record between two large-volume eruptions.

However, temporal gaps may be a function of an incomplete record: Prior to the Mesa Falls eruption, only 6 small-volume lavas are known (5 post-HRT lavas and the earlier Snake River Butte lava, Christiansen, 2001). Between the MFT and LCT eruptions, around 12 lavas are known, with the uncertainty coming from the unknown number of lavas comprising the Lewis Canyon Rhyolite. Following the LCT, the youngest period of volcanism contains at least 40 separate lavas and small volume pyroclastic deposits. This suggests that either the

frequency of lavas erupted from Yellowstone has increased by a factor of 4 after the eruption of the LCT, or, as we prefer, the younger lavas are much better preserved due to a lack of later caldera-forming eruptions. Such a preservation bias remains a challenge during investigations of ~~caldera~~ cycles at caldera volcanoes.

Petrogenesis of the IPMJ series

Our detailed mineral-scale characterisation of the IPMJ record provides important constraints for rhyolite generation in Yellowstone. Here we discuss our observations from geochemistry, petrology, and isotopic studies, which together provide a framework for rhyolite petrogenesis, within which the IPMJ series may be assessed.

Glomerocrysts as recorders of melt extraction

As previously noted ~~before~~, plagioclase and pyroxenes in the IPMJ rhyolites mostly occur together in glomerocrysts. Notably, quartz and sanidine are absent in these aggregates, despite being the most abundant phases within the overall mineral assemblage (compare table 1). Being dominated by plagioclase and mafic phases with only limited groundmass (typically <20%), these crystal aggregates are necessarily less evolved in bulk composition than the lavas within which they are hosted (Fig. 11). The stark ~~incoherence~~ contrast between the bulk compositions of crystal aggregates and the host magma has been interpreted as reflecting the extraction of rhyolitic liquid from these crystal aggregates, thus rendering them cumulates (e.g. Ellis *et al.*, 2014). The lack of sanidine and quartz in these aggregates implies that these minerals predominantly crystallised after melt was extracted, leaving behind a refractory cumulate of plagioclase, pyroxene and Fe-Ti oxides (Fig. 11, compare Ellis *et al.*, 2014). The observation that sanidine and quartz occur as large, mostly euhedral to subhedral crystals, whereas smaller plagioclase and mafic minerals are often anhedral, supports this

interpretation. We note that the majority of mafic minerals show trace element patterns consistent with growth from an evolved liquid (Fig. 8), with high contents in LREE and HREE and a pronounced Eu anomaly, similar to whole rock and glass REE patterns in IPMJ rhyolites (Fig. 2). The crystal aggregates therefore record a fractionation step between two ~~rhyolitic melts~~evolved magmas.

In bulk, glass, and pyroxene compositions, all IPMJ rhyolites contain notable negative Eu anomalies (Figs. 2, 7). The rarity of plagioclase and the low Sr contents in the erupted liquids (tables 1, 2) suggest extensive removal of plagioclase at depth to decrease the bulk Sr content from the 190-680 ppm in the basalts (Doe *et al.*, 1982) to the 10-60 ppm observed in the IPMJ rhyolites. Similarly, pyroxene fractionation could account for the extremely low contents of MgO in IPMJ rhyolites in whole rock (0.01-0.12 wt% MgO, table 2) and glasses (0.03±0.02 wt% MgO).

In the Yellowstone province, identical crystal aggregates have been reported for the young post-LCT rhyolites (Girard & Stix, 2009, Watts *et al.*, 2012), the Heise eruptive centre (Watts *et al.*, 2011), in the central Snake River Plain (Cathey & Nash, 2009, Ellis & Wolff, 2012, Ellis *et al.*, 2014) and in the Jarbidge rhyolite (Brueseke *et al.*, 2014). We note that in the Yellowstone system, both low- and normal-$\delta^{18}O$ rhyolites contain these crystal aggregates and both groups have identical major and trace elemental compositions (as noted already by Hildreth *et al.*, 1984), including low Sr contents. Thus, both rhyolite groups must have experienced large-scale plagioclase and pyroxene fractionation during petrogenesis and the observed glomerocrysts may reflect a common process of crystal-liquid separation in a mush zone (Vazquez & Reid, 2002, Stelten *et al.*, 2015).

If quartz grew primarily after extraction, the time between liquid extraction from the pyroxene-plagioclase-dominated mush zone and eruption of rhyolite magma is equal to the *minimum* time for quartz to grow without intermittent resorption stages. Based on quartz sizes

and growth rates, Ellis *et al.* (2014) suggested that timescales of extraction were on the order of a few thousand years for rhyolites of the Snake River Plain. Timescales inferred in the same fashion for IPMJ rhyolites with maximum quartz sizes of 1.5-2.9 mm and growth rates of ~10^{-13} to ~10^{-14} m/s (Gualda *et al.*, 2012b) result in timescales of ~1,000-9,000 years. Such estimates are in good agreement with longevities of crystal-poor magma of ~10,000 years based on zircon chronology (Rivera *et al.*, 2014a, Wotzlaw *et al.*, 2014) and up to 9,000 years from ^{238}U-^{230}Th dating of zircon rims (Stelten *et al.*, 2015).

Compositional variability and time scales of mineral entrainment

The large inter-grain variability seen in mineral compositions and oxygen isotopes is a pervasive feature in all IPMJ rhyolites. Previously, we noted the large variability in oxygen isotopic compositions in both quartz and sanidine, with MSWD for quartz often exceeding critical MSWD values expected for a single population (Fig. 9, see also quartz results section). Large compositional differences for trace elements in sanidines and quartz (Fig. 4) and their complex, un-systematic CL zoning patterns (Figs. 4, 5) suggest that different crystals in the same unit did not share common magmatic histories. Additionally, a comparison of trace element contents such as Ba in glass with those in rims of CL-imaged sanidine grains shows that a large number of grains did not grow in equilibrium with their host melt, even if a wide range of published K_D(San-melt) values is explored (Fig. 12). Mg-numbers in clinopyroxene are similar for a majority of grains in one unit. Deviating mineral compositions in a small number of grains identify entrainment products not in equilibrium with their host melt, such as rare more mafic pyroxenes (Fig. 7). These pyroxenes could represent remnant crystals from less evolved regions of the magmatic system as indicated by their lower content in LREE (Fig. 8). Their lack of a pronounced negative Eu anomaly suggests crystallisation prior to significant plagioclase fractionation

(compare Szymanowski *et al.*, 2015). A ~~xenocrystic~~ basaltic origin is unlikely for these high-Mg# pyroxenes as Yellowstone basalts do not contain pyroxene phenocrysts (Christiansen, 2001).

Orthopyroxenes and fayalites are commonly thought to replace one another (e.g. Davidson & Lindsley, 1989) and the abundant resorption features in fayalites suggest that conditions mostly favoured the formation of Fe-rich orthopyroxene, which is abundant in both the Heise and Yellowstone volcanic fields (e.g. Christiansen, 2001, Watts *et al.*, 2011). A mafic assemblage of clinopyroxene, orthopyroxene, fayalite and hornblende, as observed in some of these lavas (table 1), reflects a disequilibrium mineral assemblage that requires late entrainment of crystals from at least one of these mineral groups.

Un-systematic zoning patterns, variable major and trace element contents and isotopic compositions, and a complex mafic mineral assemblage point out that crystals did not share a common magmatic history and that a large number of crystals probably did not grow in the melt in which they erupted. This late-stage entrainment seems to be particularly strong in units close to the MFT-related caldera, where chemically homogenous crystals of different compositions derived either from the mush or the overlying caldera roof are assembled in the same magma batch, whereas younger MJ-rhyolites contain less variable crystal populations (Fig. 12, Fig. 9 plus see comments on compositional variability between different grains of the same unit in the respective results section on different mineral groups).

The preservation of oxygen isotopic disequilibrium between quartz and sanidine crystals allows the timescales of material entrainment to be estimated. Diffusion rates for oxygen in quartz are about four magnitudes faster than those for feldspars, and quartz crystals of 4 mm diameter would be expected to have fully equilibrated at magmatic temperature after thousands of years (Bindeman, 2008 and references therein). The internal complexities observed in CL images of the quartz grains suggest a potential for dissolution and re-

precipitation processes, which can accelerate isotopic exchange. Thus, the O isotopic disequilibria indicate that quartz was added to the magma less than a few thousand years (at a maximum) prior to eruption.

The recognition of the subtly older sanidine crystals via $^{40}Ar/^{39}Ar$ single crystal geochronology also allows an estimation of the timescale of entrainment. Diffusion calculations suggest that ages of older crystals are indistinguishable from phenocrysts after residence times of 1-2 years in the magma (Gansecki *et al.*, 1996), with similar short preservation timescales reported from other studies (Renne *et al.*, 2012). The preservation of such antecrystic sanidine requires that addition occurs immediately prior to eruption. The same process causing tails of older ages in sanidine could well be responsible for compositional ranges in all mineral groups, as sanidine is unlikely to be the only antecrystic mineral sampled prior to, and during eruption.

Assimilation and crustal component

Recurring patterns of sudden drops in $\delta^{18}O$ following caldera collapse represent the major argument for bulk remelting of hydrothermally altered material (Bindeman & Valley, 2001). Extra-caldera normal-$\delta^{18}O$ rhyolites indicate that the processes responsible for the depletions are limited to the spatial extent of the caldera and directly relate to the caldera collapse. Even if magma is stored in a mush-dominated environment, the caldera collapse can be expected to bring hydrothermally altered lithologies to sufficient depths for partial or bulk remelting, thus providing a mechanism for additional entrainment of roof material that could account for the higher crystal contents (table 1) and larger compositional mineral-scale ranges observed in the units spatially associated with the caldera.

In the same manner, assimilation and remelting of hydrothermally altered roof material following caldera collapse~~The same process~~ could be responsible for adding sufficient

amounts of H_2O to the shallow parts of the magma reservoir to allow for crystallisation of hydrous amphibole and accessory biotite. While we do not attempt to speculate about the mechanisms of this process, it is noteworthy that hydrous minerals are seemingly limited to units close to the MFT-associated caldera. ~~Furthermore, the additional input of material could account for the higher crystal contents (table 1) and larger compositional mineral-scale ranges observed in these units.~~

IPMJ-like depletions in $\delta^{18}O$ are permissive of remelting and incorporation of (1) high degrees of very slightly altered materials or (2) lower degrees of more strongly altered (lower $\delta^{18}O$) protoliths. For a simple estimate, we take the lowest value advocated by Watts *et al.* (2011) for a hydrothermally altered protolithic assimilant of -1‰ and a normal-$\delta^{18}O$ rhyolite of 6.3‰ (i.e. value expected from fractionation of mantle-derived basalt), inferring that the depletions in the IPMJ series (+5.0 to +6.1‰) can be explained by ≤25% assimilation. However, the mechanistic processes of assimilating a hydrothermally altered and mineralogically complex protolith remain poorly understood. Given that hydrothermal processes produce a wide variety of alteration assemblages with bulk $\delta^{18}O$ spanning more than 10‰ and potentially being lower than the assumed value of -1 (Hildreth *et al.*, 1984), the degree of interaction with hydrothermally altered material might deviate strongly.

In terms of radiogenic isotopes, Pb isotopes from this study (Fig. 10) show little variability and are similar to those of the majority of Yellowstone rhyolites (Doe *et al.*, 1982). Even given the strong leverage provided by Wyoming craton and the fact that the low Sr contents of these rhyolites make them particularly susceptible to Sr contamination, bulk $^{87}Sr/^{86}Sr$ values for IPMJ-rhyolites vary between 0.7090 and 0.7139, only slightly higher than the most radiogenic Yellowstone basalts of 0.7089 (Doe *et al.*, 1982, Hildreth *et al.*, 1991). Thus, the rhyolites of the IPMJ series do not require significant contamination from crustal lithologies

to pass from basalt to rhyolite and small variations likely reflect minor regional differences in the magmatic source region.

A model for the Yellowstone magmatic system between 1.3 and 0.6 Ma

In the context of the parameters discussed above, we focus here on a coherent model for the evolution of the Yellowstone magmatic system during the IPMJ period of activity. We propose that during IPMJ time, the silicic magmas of the Yellowstone magmatic system are derived from small-scale magma batches residing in a long-lived crystal-rich, mushy reservoir with the crystal aggregates representing direct samples of this mushy refractory material. These aggregates (Fig. 11) contain mostly plagioclase, pyroxene and Fe-Ti oxides, suggesting that these phases dominate the mush. Aggregates from different lavas have subtly different mineral compositions being identical to the compositions of the single crystals in that lava, suggesting that some single crystals may represent disaggregated cumulate material. If silicic lavas are a true reflection of the magma compositions beneath their eruption sites, the widely dispersed, synchronous eruption of compositionally almost indistinguishable rhyolite lavas (table 2, Fig. 2) suggests the presence of a large-volume mushy source region. Small-scale compositional differences as observed in isotopes and trace elements indicate that the composition of the mush varied both laterally and with time, suggesting that the reservoir was incrementally built and subject to changes in the focus of main activity over time.

To investigate the conditions at which the erupted magmas were stored prior to eruption, we performed simulations using rhyolite-MELTS (Gualda *et al.*, 2012a). Even though the complex mineral assemblage requires some degree of disequilibrium, we can use equilibrium magmatic modelling to approximate the last stages of crystallisation before eruption because (1) recycling mainly focused on compositionally similar material, (2) entrainment of

Formatted: Justified, Space After: 0 pt, Line spacing: Double

Formatted: Font: 12 pt, English (U.K.)

Formatted: Font: 12 pt, English (U.K.)

antecrystic mineral phases (disequilibrium on trace elemental or isotopic scale) does not preclude them from being stable in the melt, and (3) true disequilibrium assemblages such as the mafic minerals make up a small fraction of the magma (table 1). ~~In terms of mineral abundances,~~ We choose Elk Butte as a starting material for rhyolite-MELTS calculations since Elk Butte represents a~~n average~~typical MJIP member in terms of mineral compositions and does not contain any non-eruption age sanidine, therefore was not significantly affected by crystal contamination. ~~, and is therefore chosen as a starting material for r-MELTS calculations.~~ As input parameters, we use a variety of combinations of pressure (0.5-5.0 kbar) and water contents (0-5 wt% H_2O) at an oxygen fugacity of QFM (supported by the observation of fayalite, quartz and magnetite in these units and in agreement with experimental data from Bolte *et al.* (2015)). Temperature input ranges start at the calculated liquidus of the assemblage and stop at 670°C with steps of 1°C. We define the solidus as the highest temperature at which ~~r-MELTS~~rhyolite-MELTS returns <1% melt.

As described above, the mineral record in MJIP rhyolites may be complex, so we focussed on a few important parameters in order to identify likely storage conditions: (1) the crystallinity of the ~~r-MELTS~~rhyolite-MELTS run should be within the range of the IPMJ lavas (60-87% melt, table 1); (2) the composition of the melt should roughly ~~correlate with results from~~correspond to glass ~~analyses~~compositions~~ for the same unit~~; (3) the composition of sanidine predicted by ~~r-MELTS~~rhyolite-MELTS should be similar to sanidine compositions ~~in the same unit~~ (Or_{57-61}). These parameters are approximated at conditions of ~870°C, ~0.8-1 kbar and ~2.~~3~~8-3.3 wt% H_2O (see figure and additional details in supplementary file). At these conditions, the mineralogy of the ~~r-MELTS~~rhyolite-MELTS output is dominated by quartz and sanidine with minor plagioclase, consistent with these phases being dominant in the mineral assemblage (table 1). The only other crystallising phase is magnetite, and the identified conditions border to the stability field of orthopyroxene. The fact that these

Formatted: Font: 12 pt, English (U.K.)
Formatted: Font: 12 pt, English (U.K.)
Formatted: Font: 12 pt, English (U.K.)
Formatted: Font: 12 pt, English (U.K.)
Formatted: Font: 12 pt, English (U.K.)
Formatted: Font: 12 pt, English (U.K.), Subscript
Formatted: Font: 12 pt, English (U.K.)
Formatted: Font: 12 pt, English (U.K.)
Formatted: Font: 12 pt, English (U.K.)
Formatted: Font: 12 pt, English (U.K.)
Formatted: Font: 12 pt, English (U.K.)
Formatted: Font: 12 pt, English (U.K.)
Formatted: Font: 12 pt, English (U.K.), Not Highlight
Formatted: Font: 12 pt, English (U.K.), Subscript, Not Highlight
Formatted: Font: 12 pt, English (U.K.), Not Highlight
Formatted: Font: 12 pt, English (U.K.)
Formatted: Font: 12 pt, English (U.K.)
Formatted: Font: 12 pt, English (U.K.), Subscript
Formatted: Font: 12 pt, English (U.K.)
Formatted: Font: 12 pt, English (U.K.)
Formatted: Font: 12 pt, English (U.K.)

compositionnditions cannot reproduce the mafic mineral assemblage is consistent with our interpretation of them originating mostly from cumulate the glomerocrysts as cumulates, which originate fromrecord an earlier petrogenetic stage (see section "Glomerocrysts as recorders of melt extraction").

A magmatic temperature of 870°C correlatesagrees extremely well the temperature inferred from sanidine-melt geothermometry (~870°C for Elk Butte, supplementary material), suggesting that thermometry on late crystallizsing sanidine and melt pairs may result in the most reliable temperature estimates. In terms of water content, the results are slightly higher than previous estimates for rhyolites of the province based on re-homogenised melt inclusions (1.5-2.0 wt.%, Befus & Gardner, 2016) and experimental petrology (1.5-2.5 wt%, Bolte *et al.*, 2015) and lower than our estimates based on plagioclase-melt hygrometry (3.6±1.1 to 5.7±1.1 wt% H_2O, see supplementary material). The latter indicates that plagioclase-melt pairs should be treated with caution due to the longer crystallization range of plagioclase compared to sanidine. Neither significant biotite nor amphibole crystallisation is observed at the identified storage conditions or any other explored combination of pressure, temperature and water content, suggesting that crystallisation of hydrous mafic minerals is driven by a combination of less evolved melt composition at an earlier petrogenetic stage andor higher water contents, or that rhyolite-MELTS is not well-calibrated for these phases at an earlier petrogenetic stage.

The pressure estimate of 1 kbar translates to a depth of approximately 4 km given the relatively low density of the crust comprised of silicic volcanics and hydrothermally altered materials. Similar pressures ranging between 0.5 and 1.5 kbar have been reported in other studies (e.g. Befus & Gardner, 2016), albeit for the younger Yellowstone volcanism. Theise pressure estimates isare slightly lower than the upper reaches of the geophysically imaged body beneath Yellowstone (8-18 km, Husen *et al.*, 2004, Lowenstern *et al.*, 2006, Chang *et*

Formatted: Font: 12 pt, English (U.K.)
Formatted: Font: 12 pt, English (U.K.)
Formatted: Font: 12 pt, English (U.K.)
Formatted: Font: 12 pt, English (U.K.), Not Highlight
Formatted: Font: 12 pt, English (U.K.), Not Highlight
Formatted: Font: 12 pt, English (U.K.)
Formatted: Font: 12 pt, English (U.K.)
Formatted: Font: 12 pt, English (U.K.)
Formatted: Font: 12 pt, English (U.K.)
Formatted: Subscript
Formatted: Font: 12 pt, English (U.K.)
Formatted: Font: 12 pt, English (U.K.)
Formatted: Font: 12 pt, English (U.K.)
Formatted: Font: 12 pt, English (U.K.)
Formatted: Font: 12 pt, English (U.K.)
Formatted: Font: 12 pt, English (U.K.)
Formatted: Font: 12 pt, English (U.K.)
Formatted: Font: 12 pt, English (U.K.)
Formatted: Font: 12 pt, English (U.K.)

al., 2007, DeNosaquo *et al.*, 2009, Chu *et al.*, 2010, Farrell *et al.*, 2014)~~Husen et al. 2004, Lowenstern et al. 2006, Chang et al. 2007, DeNosaquo et al. 2009, Chu et al., 2010, Farrell et al., 2014)~~, where the eruptible magmas would collect prior to eruption (e.g. Bachmann & Bergantz, 2004)~~. Similar pressures ranging between 0.5 and 1.5 kbar have been reported in other studies (e.g. Befus & Gardner, 2016), albeit for the younger Yellowstone volcanism.~~ Geophysical studies have long been able to detect a large low-v_p body beneath the Yellowstone volcanic field. The proportion of crystal-poor, eruptible magma has been estimated at ~15% volume via gravity measurements (Krukoski, 2002), ≤30% volume via P-wave arrival times (Chu *et al.*, 2010), and ≤35% volume via strain measurements from seiche waves on Yellowstone lake (Luttrell *et al.*, 2013)~~. Importantly, some of the estimates above are dependent upon the degree of water saturation of the magma. The occurrence of biotite and amphibole in the IPMJ mineral assemblage indicates higher water contents in these units than often assumed for typical, dry Yellowstone rhyolites.~~ Regardless of the method of study or the proportion of crystal-poor melt estimated, geophysical studies overwhelmingly support the occurrence of a crystal mush currently underlying Yellowstone. While this does not necessarily show that such a situation occurred during IPMJ times, we have no reason to believe that the volcanic system then behaved in a fundamentally different way to today.

Based on the age clustering of IPMJ rhyolites, magmatic activity occurred in discrete pulses as is clear in the post-LCT record. Reactivation of the magmatic system probably occurred due to heat transfer following recharge at larger depths (termed 'defrosting' by Mahood (1990), compare Wolff *et al.* (2015)) and is recorded in late rims in some sanidine and quartz crystals. The reverse zonation in Ba in some sanidine crystals coupled with other trace elements (Sr, Rb, Eu) suggests that these rims result from melting of sanidine and plagioclase from the cumulate pile or crystallised from less evolved rhyolite (e.g. 960 ppm Ba in Biscuit Basin flow (Christiansen, 2001) with K_D(San-melt)≈22 (Leeman & Phelps, 1981) would

Formatted: Font: 12 pt, English (U.K.)

Formatted: Font: 12 pt, English (U.K.)

Formatted: Font: 12 pt, English (U.K.)

Formatted: Font: 12 pt, English (U.K.)

allow crystallisation of sanidine with up to 21,000 ppm Ba). Significant mass transfer from replenishing magma is not favoured due to the homogeneity in Pb isotopes (Fig. 10). Crystal aggregates generally do not contain sanidine, thus the crystal aggregates could record the refractory part of the mushy reservoir after remelting of sanidine and plagioclase (Fig. 12).

As noted above, the IPMJ rhyolites show a complex mineralogical record with entrainment of various mineral phases. Within the constraints of the preserved lavas, there appears to be little obvious compositional evolution within the magmatic system during IPMJ times, with the variability occurring in a mineral group in a single unit as large as that observed through time. Although the higher variability in our dataset compared to previous studies could be due to a larger number of analyses, this variation should not be large enough to obscure possible trends, if these had the same magnitude as the clear trend towards cooler temperatures and more juvenile isotopic compositions observed in the post-LCT lavas (compare Vazquez *et al.*, 2009). The fact that there is neither a continuous evolution through time nor sudden compositional changes that could hint at the forthcoming super eruption suggests that (1) reactivation of the magmatic system occurs on a faster timescale than can be recorded in most mineral compositions or (2) a significant preservation bias hinders conclusions on possible eruption triggers, and changes might be preserved in lavas erupted between the Mt. Haynes Rhyolite and LCT, which are now hidden under younger volcanic deposits or were removed by the LCT eruption.

The limited depletion in $\delta^{18}O$ observed in the IPMJ rhyolites does not require high degrees of remelting of hydrothermally altered precursors, as is observed for post-LCT low-$\delta^{18}O$ rhyolites with diverse phenocrysts. However, a number of similarities between the IPMJ series and the later low-$\delta^{18}O$ rhyolites hint that the processes involved in petrogenesis may not be so distinct. For example, within the IPMJ series the lowest $\delta^{18}O$ magmas and those with the highest proportion of hydrous mineral phases are those spatially associated with the

MFT-related caldera. This association supports, on a smaller scale, the cannibalisation processes proposed for the youngest Yellowstone lavas. Understanding these processes fully, however, still requires a physical model for the melting of a mineralogically complex protolith with heterogeneous isotopic compositions.

Our combined data supports a petrogenesis in an incrementally-built mushy magma reservoir with compositional variations in space and time, similar to recent models of Vazquez *et al.* (2009) and Stelten *et al.* (2015) for similarly less depleted post-LCT rhyolites. While we do not find the same thermochemical trends indicating a cooling and evolving reservoir through time as is observed for the short-lived post-LCT rhyolites, we note that the compositional evolution described in these studies was revealed from 7 lavas erupted within the space of 130 ka. Only among the IP domes do, we find a similar density of deposits, and only the Mt. Haynes Rhyolite erupted within 130 ka before the LCT. Thus, the potential for direct comparison of the IPMJ period with the post-LCT record remains limited and potential precursory geochemical signals remain elusive in the IPMJ-record.

CONCLUSIONS

Our detailed mineralogical and geochemical study of the IPMJ rhyolites provides new insights into rhyolite generation in Yellowstone, complementing previous studies that focused on the youngest Yellowstone rhyolites. Multiple lines of evidence support rhyolite genesis in an incrementally-built upper crustal mush zone with remobilisation of hydrothermally altered material occurring in areas affected by caldera collapse (Fig. 13). The striking geochemical similarity of all Yellowstone rhyolites suggests fundamentally similar processes control their generation in the shallow parts of a crystal mush.

New ages via $^{40}Ar/^{39}Ar$-dating of sanidine reveal that the magmatic series IP domes and MJ rhyolites overlap by at least 66 ka. The decreased eruption frequency in the IPMJ record

suggests that large parts of the depositional record are covered by younger lava flows, prohibiting a high-enough time resolution to decipher potential precursory activity before eruption of the LCT, if time scales allow minerals to record such processes.

Detailed investigation of the mineralogy of the IPMJ rhyolites indicates a complex assemblage of minerals within the lavas, particularly in the mafic mineral assemblage. Disequilibrium in O isotopic compositions and the preservation of subtly older single crystal $^{40}Ar/^{39}Ar$ ages in sanidines in most Yellowstone rhyolites are consistent with late stage entrainment of compositionally similar material. We infer that the processes giving rise to the variability in sanidine also generate the disequilibrium seen in other minerals. Since there is no correlation between the amount of entrained material and the eruption style, this late stage contamination likely occurs in shallow, cooler portions of the crystal mush and is enhanced in the area of the preceding caldera collapse. Here, mushy roof material could be brought to sufficient depths to be remobilised and recycled. Additional research should be undertaken to assess the preservation potential of antecrystic sanidine in mush-like conditions, with or without partial re-equilibration.

An important conclusion of this work is that trace elements and isotopes suggest that significant proportions of the crystals found within the IPMJ suite of lavas did not crystallise from the magma with which they erupted, even if the same mineral phase can be stabilised in the melt according to equilibrium magma modelling via rhyolite-MELTS. This appreciation is particularly relevant for the derivation of magmatic parameters and in-situ studies (e.g. melt inclusion or diffusion timescale work), which necessarily investigate a limited number of grains due to the time-consuming nature of the work. In such cases, conclusions derived from a small number of grains must be exported to whole magmatic systems with care.

Plagioclase-pyroxene-dominated glomerocrysts represent direct petrological samples from an underlying crystal-rich mushy zone at depth (Fig. 11). Such crystal aggregates occur in both

low-$\delta^{18}O$ rhyolites such as the Upper Basin Member rhyolites (Girard & Stix, 2009, Watts *et al.*, 2012) and the mildly depleted rhyolites of the IPMJ series, and thus represent a common part of rhyolite petrogenesis. Depletions in Sr and Eu in whole rock and glass data support significant plagioclase fractionation at depth, coherent with the scarcity of glomerocryst-forming minerals in hand specimen. While plagioclase and mafic minerals remain trapped at depth and are rarely observed in the erupted magmas, subhedral to euhedral sanidine and quartz grow after extraction of the melt. The timescales for liquid extraction from an upper crustal mush zone as inferred from quartz growth are on the order of 10 ky, consistent with timescales from zircon chronology for both effusive and explosive eruptions in Yellowstone (Rivera *et al.*, 2014a, Wotzlaw *et al.*, 2014, Stelten *et al.*, 2015).

Mafic minerals containing lower amounts of LREE and lacking a prominent Eu anomaly could represent glimpses into deeper, less evolved parts of the magmatic system, which are usually not sampled due to the sheer size of the magmatic reservoir (estimated today to be as large as c. 4000 km^3 with 5-15% melt, Farrell *et al.* (2014)). The fact that similar lavas are recurrently produced throughout the entire magmatic history of the volcanic field supports magma genesis in a coherent crystal mush via several melt-rich magma batches that may erupt independently of each other.

ACKNOWLEDGEMENTS

We thank Peter Appel and Barbara Mader (University of Kiel) for help with EMP analyses, Karsten Kunze and the Scientific Center for Optical and Electron Microscopy (ScopeM) at ETH for support with CL images, and Christie Hendrix and Stacey Gunther from the Yellowstone National Park Service for their assistance with research permits (Yellowstone permit YELL-05940). We are grateful to Mark Stelten, Christy Till and James Brophy for their constructive and careful reviews. Wendy Bohrson is thanked for editorial handling and

providing additional helpful comments on the manuscript. This work was supported by an ETH research grant (ETH-05 13-2 to J.T.), funds from Swiss National Science Foundation research grants (SNSF 200021-146268 and SNSF 200021-155923/1 covering O.B. and B.S.E.), an ETH student research travel fund (to J.T.) and an American Philosophical Society Franklin Grant (to B.S.E.).

REFERENCES

Almeev, R. R., Bolte, T., Nash, B. P., Holtz, F., Erdmann, M. & Cathey, H. E. (2012). High-temperature, low-H_2O silicic magmas of the Yellowstone hotspot: an experimental study of rhyolite from the Bruneau–Jarbidge Eruptive Center, Central Snake River Plain, USA. *Journal of Petrology* **53**, 1837-1866.

Bachmann, O. & Bergantz, G. W. (2004). On the origin of crystal-poor rhyolites: extracted from batholithic crystal mushes. *Journal of Petrology* **45**, 1565-1582.

Befus, K. S. & Gardner, J. E. (2016). Magma storage and evolution of the most recent effusive and explosive eruptions from Yellowstone Caldera. *Contributions to Mineralogy and Petrology* **171**, 1-19.

Bindeman, I. (2008). Oxygen isotopes in mantle and crustal magmas as revealed by single crystal analysis. *Reviews in Mineralogy and Geochemistry* **69**, 445-478.

Bindeman, I. N., Fu, B., Kita, N. T. & Valley, J. W. (2008). Origin and Evolution of Silicic Magmatism at Yellowstone Based on Ion Microprobe Analysis of Isotopically Zoned Zircons. *Journal of Petrology* **49**, 163-193.

Bindeman, I. N. & Valley, J. W. (2001). Low-$\delta^{18}O$ Rhyolites from Yellowstone: Magmatic evolution based on analyses of Zircons and individual phenocrysts. *Journal of Petrology* **42**, 1491-1517.

Boehnke, P., Watson, E. B., Trail, D., Harrison, T. M. & Schmitt, A. K. (2013). Zircon saturation re-revisited. *Chemical geology* **351**, 324-334.

Bolte, T., Holtz, F., Almeev, R. & Nash, B. (2015). The Blacktail Creek Tuff: an analytical and experimental study of rhyolites from the Heise volcanic field, Yellowstone hotspot system. *Contributions to Mineralogy and Petrology* **169**, 1-24.

Brueseke, M. E., Callicoat, J. S., Hames, W. & Larson, P. B. (2014). Mid-Miocene rhyolite volcanism in northeastern Nevada: The Jarbidge Rhyolite and its relationship to the Cenozoic evolution of the northern Great Basin (USA). *Geological Society of America Bulletin*, B30736. 30731.

Cathey, H. E. & Nash, B. P. (2009). Pyroxene thermometry of rhyolite lavas of the Bruneau–Jarbidge eruptive center, Central Snake River Plain. *Journal of Volcanology and Geothermal Research* **188**, 173-185.

Chang, W.-L., Smith, R. B., Wicks, C., Farrell, J. M. & Puskas, C. M. (2007). Accelerated uplift and magmatic intrusion of the Yellowstone caldera, 2004 to 2006. *Science* **318**, 952-956.

Christiansen, R. L. (1984). Yellowstone magmatic evolution: Its bearing on understanding large-volume explosive volcanism. *Explosive volcanism: inception, evolution, and hazards*, 84-95.

Christiansen, R. L. (2001). *The Quaternary and Pliocene Yellowstone Plateau Volcanic Field of Wyoming, Idaho, and Montana*: USGS.

Christiansen, R. L. & Blank, H. R. (1972). Volcanic stratigraphy of the Quaternary rhyolite plateau in Yellowstone National Park. *USGS Professional Papers* **729-B**.

Christiansen, R. L. L., Jacob B.; Smith, Robert B.; Heasler, Henry; Morgan, Lisa A.; Nathenson, Manuel; Mastin, Larry G.; Muffler, L. J. Patrick; Robinson, Joel E. (2007). Preliminary Assessment of Volcanic and Hydrothermal Hazards in Yellowstone National Park and vicinity. *USGS Open-file report*: USGS.

Formatted: Font: (Default) Times New Roman

Chu, R., Helmberger, D. V., Sun, D., Jackson, J. M. & Zhu, L. (2010). Mushy magma beneath Yellowstone. *Geophysical Research Letters* **37**.

Coble, M. A. & Mahood, G. A. (2012). Initial impingement of the Yellowstone plume located by widespread silicic volcanism contemporaneous with Columbia River flood basalts. *Geology* **40**, 655-658.

Dallegge, T. A. (2008). 40Ar/39Ar Geochronology of lavas from the Central Plateau Member of Plateau Rhyolite with implications for magma residence times and eruptive reoccurrence intervals, Yellowstone National Park.

Davidson, P. M. & Lindsley, D. H. (1989). Thermodynamic analysis of pyroxene-olivine-quartz equilibria in the system CaO-MgO-FeO-SiO 2. *American Mineralogist* **74**, 18-30.

DeNosaquo, K. R., Smith, R. B. & Lowry, A. R. (2009). Density and lithospheric strength models of the Yellowstone–Snake River Plain volcanic system from gravity and heat flow data. *Journal of Volcanology and Geothermal Research* **188**, 108-127.

Doe, B. R., Leeman, W. P., Christiansen, R. L. & Hedge, C. E. (1982). Lead and strontium isotopes and related trace elements as genetic tracers in the Upper Cenozoic rhyolite-basalt association of the Yellowstone Plateau Volcanic Field. *Journal of Geophysical Research: Solid Earth* **87**, 4785-4806.

Ellis, B., Wolff, J., Boroughs, S., Mark, D., Starkel, W. & Bonnichsen, B. (2013). Rhyolitic volcanism of the central Snake River Plain: a review. *Bulletin of Volcanology* **75**, 1-19.

Ellis, B. S., Bachmann, O. & Wolff, J. A. (2014). Cumulate fragments in silicic ignimbrites: The case of the Snake River Plain. *Geology* **42**, 431-434.

Ellis, B. S., Mark, D. F., Pritchard, C. J. & Wolff, J. A. (2012). Temporal dissection of the Huckleberry Ridge Tuff using the $^{40}Ar/^{39}Ar$ dating technique. *Quaternary Geochronology* **9**, 34-41.

Ellis, B. S. & Wolff, J. A. (2012). Complex storage of rhyolite in the central Snake River Plain. *Journal of Volcanology and Geothermal Research* **211**, 1-11.

Farrell, J., Smith, R. B., Husen, S. & Diehl, T. (2014). Tomography from 26 years of seismicity revealing that the spatial extent of the Yellowstone crustal magma reservoir extends well beyond the Yellowstone caldera. *Geophysical Research Letters*.

Gansecki, C., Mahood, G. & McWilliams, M. (1998). New ages for the climactic eruptions at Yellowstone: single-crystal $^{40}Ar/^{39}Ar$ dating identifies contamination. *Geology* **26**, 343-346.

Gansecki, C. A., Mahood, G. A. & McWilliams, M. O. (1996). $^{40}Ar/^{39}Ar$ geochronology of rhyolites erupted following collapse of the Yellowstone caldera, Yellowstone Plateau volcanic field: implications for crustal contamination. *Earth and Planetary Science Letters* **142**, 91-107.

Geist, D. & Richards, M. (1993). Origin of the Columbia Plateau and Snake River plain: Deflection of the Yellowstone plume. *Geology* **21**, 789-792.

Girard, G. & Stix, J. (2009). Magma Recharge and Crystal Mush Rejuvenation Associated with Early Post-collapse Upper Basin Member Rhyolites, Yellowstone Caldera, Wyoming. *Journal of Petrology* **50**, 2095-2125.

Girard, G. & Stix, J. (2010). Rapid extraction of discrete magma batches from a large differentiating magma chamber: the Central Plateau Member rhyolites, Yellowstone Caldera, Wyoming. *Contributions to Mineralogy and Petrology* **160**, 441-465.

Gualda, G. A., Ghiorso, M. S., Lemons, R. V. & Carley, T. L. (2012a). Rhyolite-MELTS: a modified calibration of MELTS optimized for silica-rich, fluid-bearing magmatic systems. *Journal of Petrology* **53**, 875-890.

Gualda, G. A., Pamukcu, A. S., Ghiorso, M. S., Anderson Jr, A. T., Sutton, S. R. & Rivers, M. L. (2012b). Timescales of quartz crystallization and the longevity of the Bishop giant magma body. *PloS one* **7**, e37492.

Guillong, M., Meier, D., Allan, M., Heinrich, C. & Yardley, B. (2008). SILLS: a MATLAB-based program for the reduction of laser ablation ICP-MS data of homogeneous materials and inclusions. *Mineralogical Association of Canada Short Course* **40**, 328-333.

Hanchar, J. M. & Watson, E. B. (2003). Zircon saturation thermometry. *Reviews in Mineralogy and Geochemistry* **53**, 89-112.

Hildreth, W., Christiansen, R. L. & O'Neil, J. R. (1984). Catastrophic isotopic modification of rhyolitic magma at times of caldera subsidence, Yellowstone Plateau Volcanic Field. *Journal of Geophysical Research* **89**, 8339.

Hildreth, W., Halliday, A. N. & Christiansen, R. L. (1991). Isotopic and Chemical Evidence Concerning the Genesis and Contamination of Basaltic and Rhyolitic Magma Beneath the Yellowstone Plateau Volcanic Field. *Journal of Petrology* **32**, 63-138.

Hildreth, W. & Wilson, C. J. (2007). Compositional zoning of the Bishop Tuff. *Journal of Petrology* **48**, 951-999.

Hooper, P. R., Camp, V. E., Reidel, S. P. & Ross, M. E. (2007). The origin of the Columbia River flood basalt province: Plume versus nonplume models. *Geological Society of America Special Papers* **430**, 635-668.

Husen, S., Smith, R. B. & Waite, G. P. (2004). Evidence for gas and magmatic sources beneath the Yellowstone volcanic field from seismic tomographic imaging. *Journal of Volcanology and Geothermal Research* **131**, 397-410.

Hynek, S. A., Brown, F. H. & Fernandez, D. P. (2011). A rapid method for hand picking potassium-rich feldspar from silicic tephra. *Quaternary Geochronology* **6**, 285-288.

Johnson, D., Hooper, P. & Conrey, R. (1999). XRF analysis of rocks and minerals for major and trace elements on a single low dilution Li-tetraborate fused bead. *Advances in X-ray Analysis, v, 41, p. 843–867 Le Bas, MJ*: Citeseer.

Kent, A. J. R. (2008). In-situ analysis of Pb isotope ratios using laser ablation MC-ICP-MS: Controls on precision and accuracy and comparison between Faraday and ion counting systems. *Journal of Analytical Atom Spectrometry* **23**, 968-975.

Krukoski, J. C. (2002). A geologic data base (GeoGIS) and three-dimensional inversion for the density structure of the Yellowstone volcanic system. M.S. thesis. University of Utah, 96 pp.

Lanphere, M. A., Champion, D. E., Christiansen, R. L., Izett, G. A. & Obradovich, J. D. (2002). Revised ages for tuffs of the Yellowstone Plateau volcanic field: Assignment of the Huckleberry Ridge Tuff to a new geomagnetic polarity event. *Geological Society of America Bulletin* **114**, 559-568.

Lee, J.-Y., Marti, K., Severinghaus, J. P., Kawamura, K., Yoo, H.-S., Lee, J. B. & Kim, J. S. (2006). A redetermination of the isotopic abundances of atmospheric Ar. *Geochimica et Cosmochimica Acta* **70**, 4507-4512.

Leeman, W. P., MacRae, C. M., Wilson, N. C., Torpy, A., Lee, C. T., Student, J. J., Thomas, J. B. & Vicenzi, E. P. (2012). A study of cathodoluminescence and trace element compositional zoning in natural quartz from volcanic rocks: mapping titanium content in quartz. *Microsc Microanal* **18**, 1322-1341.

Leeman, W. P. & Phelps, D. W. (1981). Partitioning of rare earths and other trace elements between sanidine and coexisting volcanic glass. *Journal of Geophysical Research* **86**, 10193-10199.

Lowenstern, J. B., Smith, R. B. & Hill, D. P. (2006). Monitoring super-volcanoes: geophysical and geochemical signals at Yellowstone and other large caldera systems. *Philos Trans A Math Phys Eng Sci* **364**, 2055-2072.

Luttrell, K., Mencin, D., Francis, O. & Hurwitz, S. (2013). Constraints on the upper crustal magma reservoir beneath Yellowstone Caldera inferred from lake-seiche induced strain observations. *Geophysical Research Letters* **40**, 501-506.

Mahood, G. (1990). Second reply to comment of RSJ Sparks, HE Huppert and CJN Wilson on "Evidence for long residence times of rhyolitic magma in the Long Valley magmatic system: the isotopic record in the precaldera lavas of Glass Mountain". *Earth and Planetary Science Letters* **99**, 395-399.

Mahood, G. & Hildreth, W. (1983). Large partition coefficients for trace elements in high-silica rhyolites. *Geochimica et Cosmochimica Acta* **47**, 11-30.

Mark, D., Renne, P., Morgan, L., Deino, A., Smith, V., Ellis, B. & Pearce, N. (2012). 40Ar/39Ar dating of Pleistocene tuffs: an accurate age for the Matuyama-Brunhes geomagnetic reversal (MBGR). *AGU Fall Meeting Abstracts* **1**, 07.

Mark, D., Stuart, F. & De Podesta, M. (2011). New high-precision measurements of the isotopic composition of atmospheric argon. *Geochimica et Cosmochimica Acta* **75**, 7494-7501.

Mark, D. F., Parnell, J., Kelley, S. P., Lee, M., Sherlock, S. C. & Carr, A. (2005). Dating of multistage fluid flow in sandstones. *Science* **309**, 2048-2051.

Matthews, N. E., Vazquez, J. A. & Calvert, A. T. (2015). Age of the Lava Creek supereruption and magma chamber assembly at Yellowstone based on 40Ar/39Ar and U-Pb dating of sanidine and zircon crystals. *Geochemistry, Geophysics, Geosystems* **16**, 2508-2528.

McDonough, W. F. & Sun, S.-S. (1995). The composition of the Earth. *Chemical geology* **120**, 223-253.

Minnis, P., Harrison, E., Stowe, L., Gibson, G., Denn, F., Doelling, D. & Smith, W. (1993). Radiative climate forcing by the Mount Pinatubo eruption. *Science* **259**, 1411-1415.

Morgan, L., Mark, D., Imlach, J., Barfod, D. & Dymock, R. (2014). FCs-EK: a new sampling of the Fish Canyon Tuff 40Ar/39Ar neutron flux monitor. *Geological Society, London, Special Publications* **378**, 63-67.

Obradovich, J. D. (1992). Geochronology of the Late Cenozoic volcanism of Yellowstone National Park and adjoining areas, Wyoming and Idaho. *Open-File Report*: USGS, 45.

Putirka, K. D. (2008). Thermometers and barometers for volcanic systems. *Reviews in Mineralogy and Geochemistry* **69**, 61-120.

Renne, P. R., Balco, G., Ludwig, K. R., Mundil, R. & Min, K. (2011). Response to the comment by WH Schwarz et al. on "Joint determination of 40K decay constants and 40Ar∗/40K for the Fish Canyon sanidine standard, and improved accuracy for 40Ar/39Ar geochronology" by PR Renne et al.(2010). *Geochimica et Cosmochimica Acta* **75**, 5097.

Renne, P. R., Deino, A. L., Hames, W. E., Heizler, M. T., Hemming, S. R., Hodges, K. V., Koppers, A. A., Mark, D. F., Morgan, L. E. & Phillips, D. (2009). Data reporting norms for $^{40}Ar/^{39}Ar$ geochronology. *Quaternary Geochronology* **4**, 346-352.

Renne, P. R., Mulcahy, S. R., Cassata, W. S., Morgan, L. E., Kelley, S. P., Hlusko, L. J. & Njau, J. K. (2012). Retention of inherited Ar by alkali feldspar xenocrysts in a magma: Kinetic constraints from Ba zoning profiles. *Geochimica et Cosmochimica Acta* **93**, 129-142.

Renne, P. R., Mundil, R., Balco, G., Min, K. & Ludwig, K. R. (2010). Joint determination of ^{40}K decay constants and $^{40}Ar*/^{40}K$ for the Fish Canyon sanidine standard, and improved accuracy for $^{40}Ar/^{39}Ar$ geochronology. *Geochimica et Cosmochimica Acta* **74**, 5349.

Rivera, T. A., Schmitz, M. D., Crowley, J. L. & Jicha, B. R. (2014a). Longevity of the Mesa Falls Tuff magma system recorded by zircon petrochronology and sanidine $^{40}Ar/^{39}Ar$ dates. *GSA Annual Meeting*. Vancouver.

Rivera, T. A., Schmitz, M. D., Crowley, J. L. & Storey, M. (2014b). Rapid magma evolution constrained by zircon petrochronology and 40Ar/39Ar sanidine ages for the Huckleberry Ridge Tuff, Yellowstone, USA. *Geology* **42**, 643-646.

Self, S. (2006). The effects and consequences of very large explosive volcanic eruptions. *Philosophical Transactions of the Royal Society A: Mathematical, Physical and Engineering Sciences* **364**, 2073-2097.

Simakin, A. & Bindeman, I. (2012). Remelting in caldera and rift environments and the genesis of hot,"recycled" rhyolites. *Earth and Planetary Science Letters* **337**, 224-235.

Stelten, M. E., Cooper, K. M., Vazquez, J. A., Calvert, A. T. & Glessner, J. J. (2015). Mechanisms and Timescales of Generating Eruptible Rhyolitic Magmas at Yellowstone Caldera from Zircon and Sanidine Geochronology and Geochemistry. *Journal of Petrology*, egv047.

Szymanowski, D., Ellis, B. S., Bachmann, O., Guillong, M. & Phillips, W. M. (2015). Bridging basalts and rhyolites in the Yellowstone–Snake River Plain volcanic province: The elusive intermediate step. *Earth and Planetary Science Letters* **415**, 80-89.

Thomas, J. B. & Watson, E. B. (2012). Application of the Ti-in-quartz thermobarometer to rutile-free systems. Reply to: a comment on:'TitaniQ under pressure: the effect of pressure and temperature on the solubility of Ti in quartz'by Thomas et al. *Contributions to Mineralogy and Petrology* **164**, 369-374.

Vazquez, J. A., Kyriazis, S. F., Reid, M. R., Sehler, R. C. & Ramos, F. C. (2009). Thermochemical evolution of young rhyolites at Yellowstone: Evidence for a cooling but periodically replenished postcaldera magma reservoir. *Journal of Volcanology and Geothermal Research* **188**, 186-196.

Vazquez, J. A. & Reid, M. R. (2002). Time scales of magma storage and differentiation of voluminous high-silica rhyolites at Yellowstone caldera, Wyoming. *Contributions to Mineralogy and Petrology* **144**, 274-285.

Wark, D. A. & Watson, E. B. (2006). TitaniQ: a titanium-in-quartz geothermometer. *Contributions to Mineralogy and Petrology* **152**, 743-754.

Watts, K. E., Bindeman, I. N. & Schmitt, A. K. (2011). Large-volume rhyolite genesis in caldera complexes of the Snake River Plain: insights from the Kilgore Tuff of the Heise Volcanic Field, Idaho, with comparison to Yellowstone and Bruneau–Jarbidge rhyolites. *Journal of Petrology* **52**, 857-890.

Watts, K. E., Bindeman, I. N. & Schmitt, A. K. (2012). Crystal scale anatomy of a dying supervolcano: an isotope and geochronology study of individual phenocrysts from voluminous rhyolites of the Yellowstone caldera. *Contributions to Mineralogy and Petrology* **164**, 45-67.

Wolff, J., Ellis, B., Ramos, F., Starkel, W., Boroughs, S., Olin, P. & Bachmann, O. (2015). Remelting of cumulates as a process for producing chemical zoning in silicic tuffs: A comparison of cool, wet and hot, dry rhyolitic magma systems. *Lithos*.

Wolff, J., Ramos, F., Hart, G., Patterson, J. & Brandon, A. (2008). Columbia River flood basalts from a centralized crustal magmatic system. *Nature geoscience* **1**, 177-180.

Wotzlaw, J.-F., Bindeman, I. N., Stern, R. A., D'Abzac, F.-X. & Schaltegger, U. (2015). Rapid heterogeneous assembly of multiple magma reservoirs prior to Yellowstone supereruptions. *Scientific reports* **5**.

Wotzlaw, J.-F., Bindeman, I. N., Watts, K. E., Schmitt, A. K., Caricchi, L. & Schaltegger, U. (2014). Linking rapid magma reservoir assembly and eruption trigger mechanisms at evolved Yellowstone-type supervolcanoes. *Geology*, G35979. 35971.

Formatted: Left, Indent: Left: 0", Hanging: 0.49", Space After: 0 pt, Don't add space between paragraphs of the same style, Don't swap indents on facing pages

Figure captions

Fig. 1: Distribution of IPMJ rhyolites in the Yellowstone area after geological map of Christiansen (2001). IP domes are shown in purple, MJ lavas in green and the Lewis Canyon Rhyolite in dark green. Dashed red lines indicate approximate caldera outlines related to eruption of HRT (I), MFT (II) and LCT (III). Black dashed line shows borders of Yellowstone National Park. Upper left inset shows unit abbreviations and affiliation of units with either the Island Park or Mount Jackson series. Upper right inset shows location of the Yellowstone volcanic province within North America, grey blobs mark eruptive centres along the Yellowstone hotspot track.

Fig. 2: REE contents normalised to BSE composition (McDonough & Sun, 1995) for bulk rock and glasses (grey area), where units contain glass (compare table 1). Note the strong

depletions in Ba, Sr and Eu, suggestive of extensive plagioclase fractionation. Depletions for glass are more pronounced due to sanidine and plagioclase in whole rock.

Fig. 3: Spatial distribution and appearance of IPMJ rhyolites based on $^{40}Ar/^{39}Ar$-eruption ages determined on sanidine. Coloured regions connect units from the same syn-eruptive cluster as marked with a frame in bottom panel. Bottom panel shows eruption age as stated in table 3 with error bars marking the full external precision (2 sigma, see text), noted in grey are the two rhyolites not covered in this study: FM = Flat Mountain Rhyolite at c. 0.93 Ma K-Ar age from Obradovich (1992), BB = Big Bear Lake flow (undated, probable age based on stratigraphic relationships as recommended by Christiansen *et al.* (2001)). Ins~~l~~et diagrams show~~s~~ frequency distributions for some typical units, with the black solid line marking the distribution of eruption age grains ~~note the preservation of non-eruptive ages~~and the black dashed line the preservation of non-eruptive ages.

Fig. 4: Cathodoluminescence images o~~f~~n quartz crystals sorted by eruption age (top left to bottom right young to old). Titanium concentrations (ppm) measured by LA-ICPMS are listed next to analysis locations (white circles). Bottom panel shows relative probability distributions of Ti concentrations in quartz grains from each unit and the number of analyses. Note the higher Ti contents in the Lewis Canyon Rhyolite compared to other MJ lavas.

Fig. 5: CL images of typical sanidine grains with locations of trace element analysis; An-Ab-Or ternary plot of sanidines and plagioclase from the IPMJ rhyolites, grey areas mark compositions of other Yellowstone rhyolites (Hildreth *et al.*, 1984, Gansecki *et al.*, 1996).

Fig. 6: Examples of mafic minerals in back-scatter images (from upper left to bottom right): 1) exsolved magnetite, 2) clinopyroxene with zircon and apatite inclusions, 3) resorbed fayalite, 4) subhedral Fe-hornblende, 5) subhedral orthopyroxene with Fe-Ti inclusions, 6) "fresh" anhedral inclusion-rich fayalite, 7) clinopyroxene overgrowth of orthopyroxene, 8) euhedral fresh clinopyroxene, 9) resorbed fayalite with cracks.

Fig. 7: Pyroxene compositions from the MJ rhyolites (left) and the IP domes (right) illustrating the wide compositional range between pyroxenes within the same unit.

Fig. 8: REE contents in mafic minerals normalised to BSE composition (McDonough & Sun, 1995). Dark grey fields show REE patterns of the majority of crystals, likely to have grown in a highly evolved rhyolitic melt. Black lines indicate REE contents of crystals deviating from the main trend. Crystals depleted in LREE and lacking characteristic Eu anomaly crystallised in less evolved magma prior to significant plagioclase fractionation. ~~Non parallel patterns suggest that parts of the mineral fraction are not co-genetic emphasising the complexity in the crystal heritage.~~

Fig. 9: Oxygen isotopes $\delta^{18}O$ in ‰ VSMOW for explosive end members MFT and LCT and effusive domes and lavas in-between (abbreviations and colours as in Fig. 1). Wide boxes indicate probable $\delta^{18}O_{melt}$ values calculated from average quartz compositions for each unit. Grey background bar illustrates range of "normal"-$\delta^{18}O$ rhyolites (expected values by fractionation of MOR and arc basalts, Bindeman (2008) and references therein). Upper panel defines the MSWD of the quartz analyses. MSWD > $MSWD_{critical}$ indicates that the results do not represent a single population. Lower panel represents trends in $\delta^{18}O$ throughout the

history of the Yellowstone volcanic field (after Bindeman and Valley, 2001; Hildreth et al. 1984).

Fig. 10: Pb isotopes in sanidine in IPMJ rhyolites. Inlet diagram shows the entire range of Pb isotopic compositions for the entire Yellowstone volcanic field with red-framed box showing the extent of main diagram. Data for IPMJ rhyolites from this study, MFT from Ellis et al. (unpublished data), other Yellowstone rhyolites and basalts from Doe et al. (1982); Watts et al. (2012).

Fig. 11: Example of glomerocrysts from different Island Park domes. Comparison of mineral assemblage within the aggregate with free single crystals yields no significant compositional differences. Bulk glomerocryst compositions are less evolved compared to typical whole rock modal compositions due to the lack of late-forming sanidine and quartz.

Fig. 12: (A) Ba contents in sanidine rims and cores do not fall into the calculated equilibrium range expected from Ba contents in glass from the same unit. Equilibrium range calculated with K_D(San-melt)≈22 in rhyolite from Leeman and Phelps (1981) and K_D(San-melt)≈6.7 in high-silica rhyolite (Mahood & Hildreth, 1983). Figure contains only data for those sanidine crystals that were imaged via CL. (B) Average Rb/Sr in San for each unit with error bars indicating one standard deviation. Numbers in italic correspond to number of analyses per unit. Note the large variability for IP domes and Moose Creek (MC) compared to MJ flows, indicating higher entrainment component for units close to MFT-related caldera. (C) Ba ratio between rim and core and Sr ratio respectively suggest that reverse zoning in San is due to cumulate remelting or crystallisation from less evolved rhyolite melt. Figure contains only data for those sanidine crystals that were imaged via CL.

Fig. 13: Schematic summary diagram of petrogenetic processes and characteristics of the IPMJ rhyolite series.

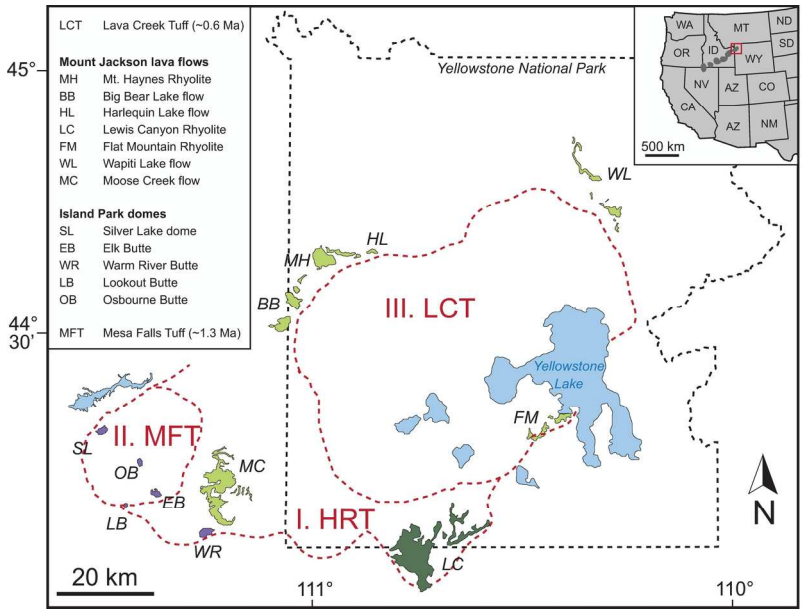

Fig. 1: Distribution of IPMJ rhyolites in the Yellowstone area after geological map of Christiansen (2001). IP domes are shown in purple, MJ lavas in green and the Lewis Canyon Rhyolite in dark green. Dashed red lines indicate approximate caldera outlines related to eruption of HRT (I), MFT (II) and LCT (III). Black dashed line shows borders of Yellowstone National Park. Upper left inset shows unit abbreviations and affiliation of units with either the Island Park or Mount Jackson series. Upper right inset shows location of the Yellowstone volcanic province within North America, grey blobs mark eruptive centres along the Yellowstone hotspot track.

Fig. 1
175x105mm (300 x 300 DPI)

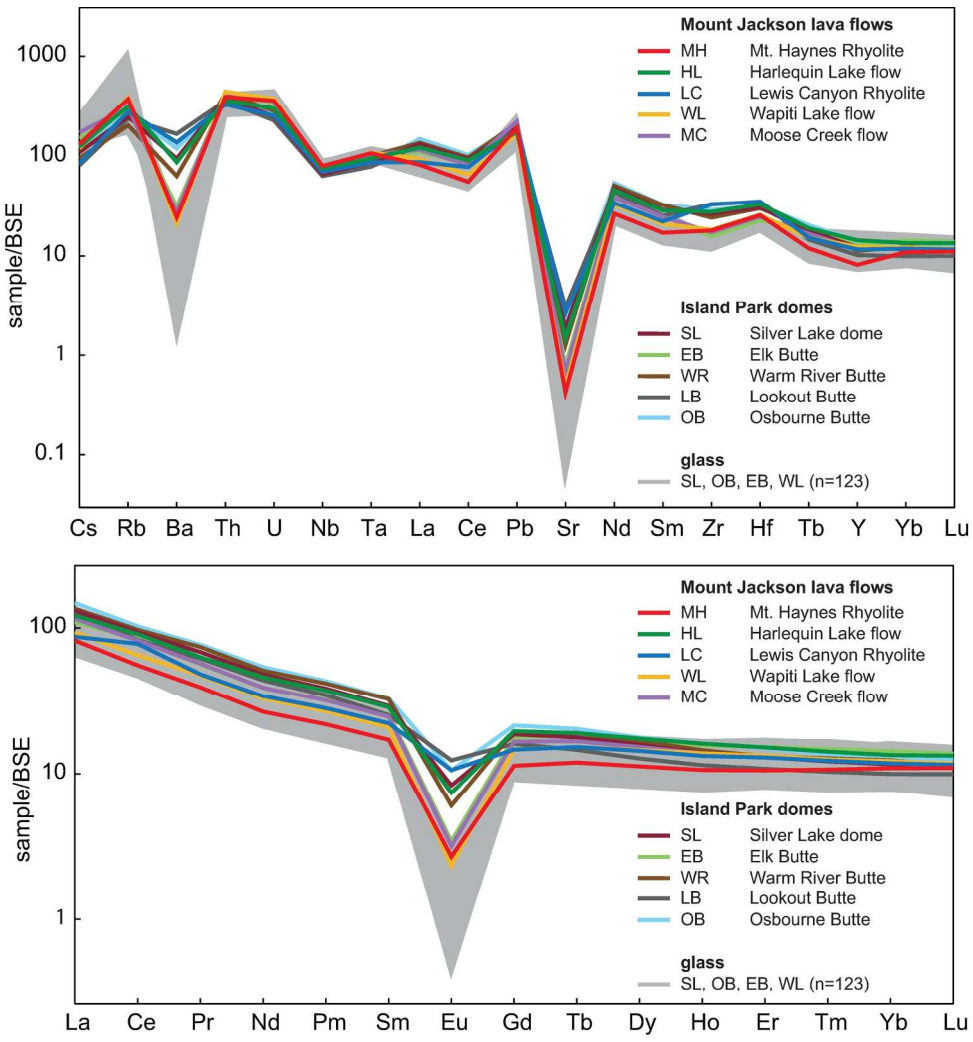

Fig. 2: REE contents normalised to BSE composition (McDonough & Sun, 1995) for bulk rock and glasses (grey area), where units contain glass (compare table 1). Note the strong depletions in Ba, Sr and Eu, suggestive of extensive plagioclase fractionation. Depletions for glass are more pronounced due to sanidine and plagioclase in whole rock.

Fig. 2
198x213mm (300 x 300 DPI)

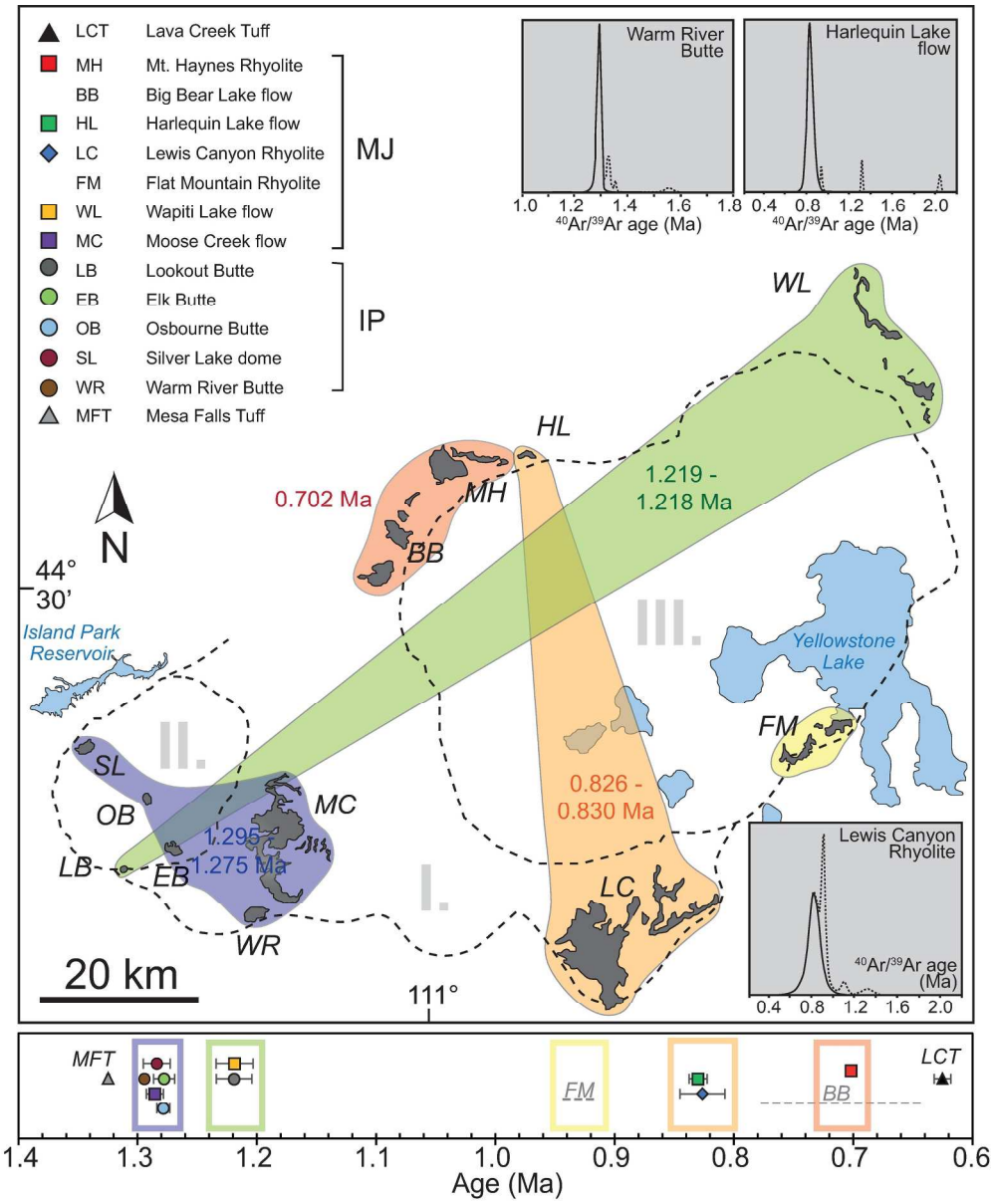

Fig. 3: Spatial distribution and appearance of IPMJ rhyolites based on $^{40}Ar/^{39}Ar$-eruption ages determined on sanidine. Coloured regions connect units from the same syn-eruptive cluster as marked with a frame in bottom panel. Bottom panel shows eruption age as stated in table 3 with error bars marking the full external precision (2 sigma, see text), noted in grey are the two rhyolites not covered in this study: FM = Flat Mountain Rhyolite at c. 0.93 Ma K-Ar age from Obradovich (1992), BB = Big Bear Lake flow (undated, probable age based on stratigraphic relationships as recommended by Christiansen et al. (2001)). Inset diagrams show frequency distributions for some typical units, with the black solid line marking the distribution of eruption age grains and the black dashed line the preservation of non-eruptive ages.

Fig. 3
216x261mm (300 x 300 DPI)

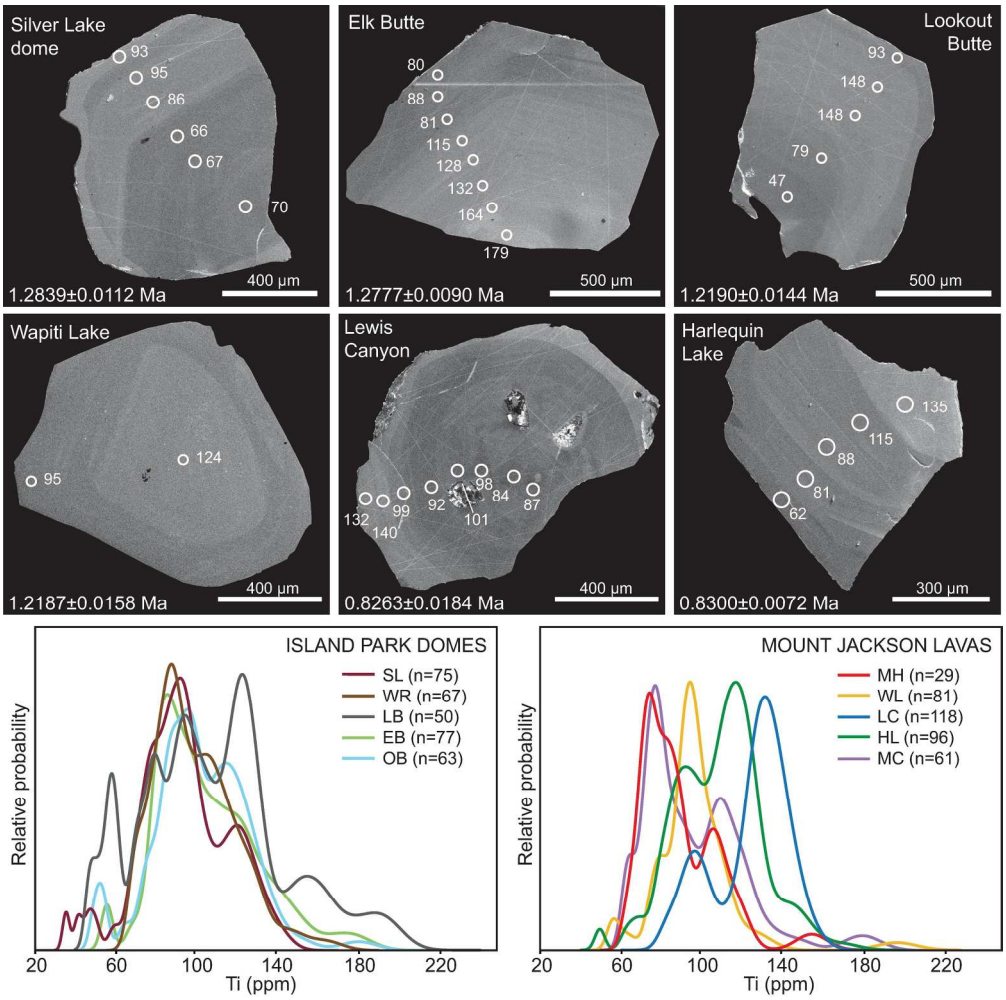

Fig. 4: Cathodoluminescence images of quartz crystals sorted by eruption age (top left to bottom right young to old). Titanium concentrations (ppm) measured by LA-ICPMS are listed next to analysis locations (white circles). Bottom panel shows relative probability distributions of Ti concentrations in quartz grains from each unit and the number of analyses. Note the higher Ti contents in the Lewis Canyon Rhyolite compared to other MJ lavas.

Fig. 4

199x197mm (300 x 300 DPI)

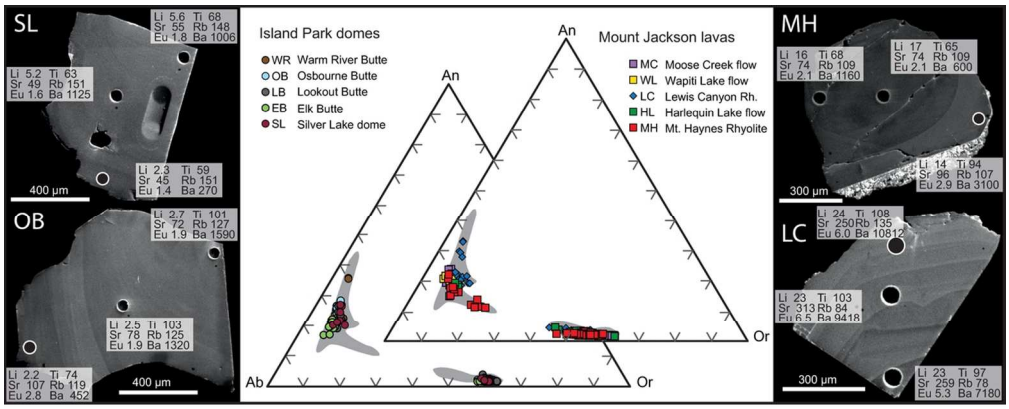

Fig. 5: CL images of typical sanidine grains with locations of trace element analysis; An-Ab-Or ternary plot of sanidines and plagioclase from the IPMJ rhyolites, grey areas mark compositions of other Yellowstone rhyolites (Hildreth et al., 1984, Gansecki et al., 1996).
Fig. 5
116x49mm (300 x 300 DPI)

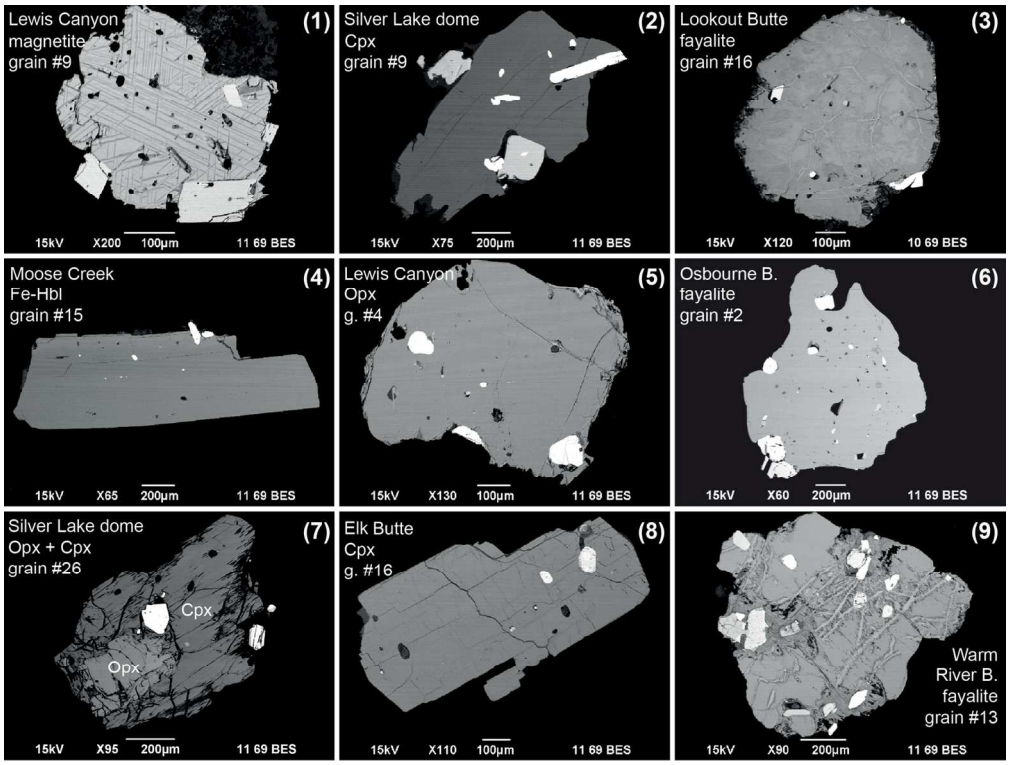

Fig. 6: Examples of mafic minerals in back-scatter images (from upper left to bottom right): 1) exsolved magnetite, 2) clinopyroxene with zircon and apatite inclusions, 3) resorbed fayalite, 4) subhedral Fe-hornblende, 5) subhedral orthopyroxene with Fe-Ti inclusions, 6) "fresh" anhedral inclusion-rich fayalite, 7) clinopyroxene overgrowth of orthopyroxene, 8) euhedral fresh clinopyroxene, 9) resorbed fayalite with cracks.

Fig. 6

152x114mm (300 x 300 DPI)

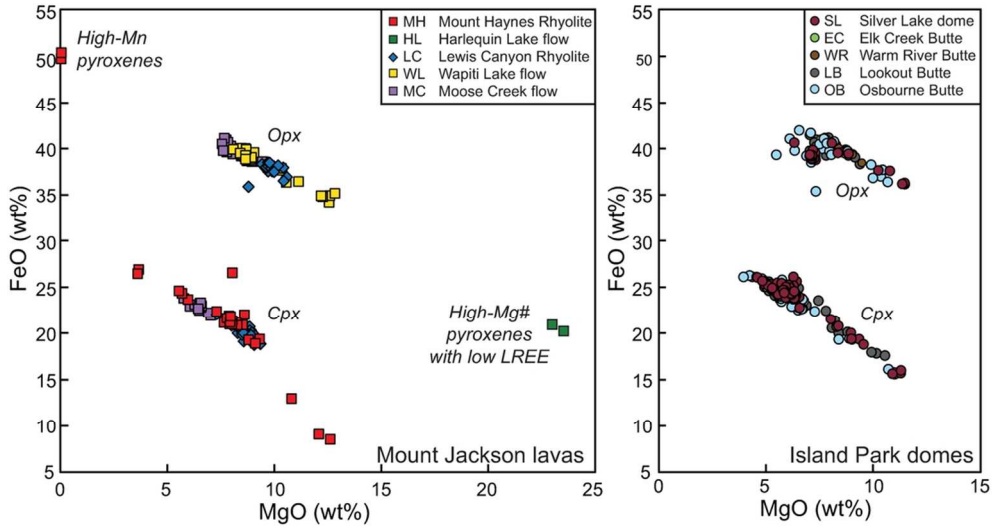

Fig. 7: Pyroxene compositions from the MJ rhyolites (left) and the IP domes (right) illustrating the wide compositional range between pyroxenes within the same unit.

Fig. 7
99x51mm (300 x 300 DPI)

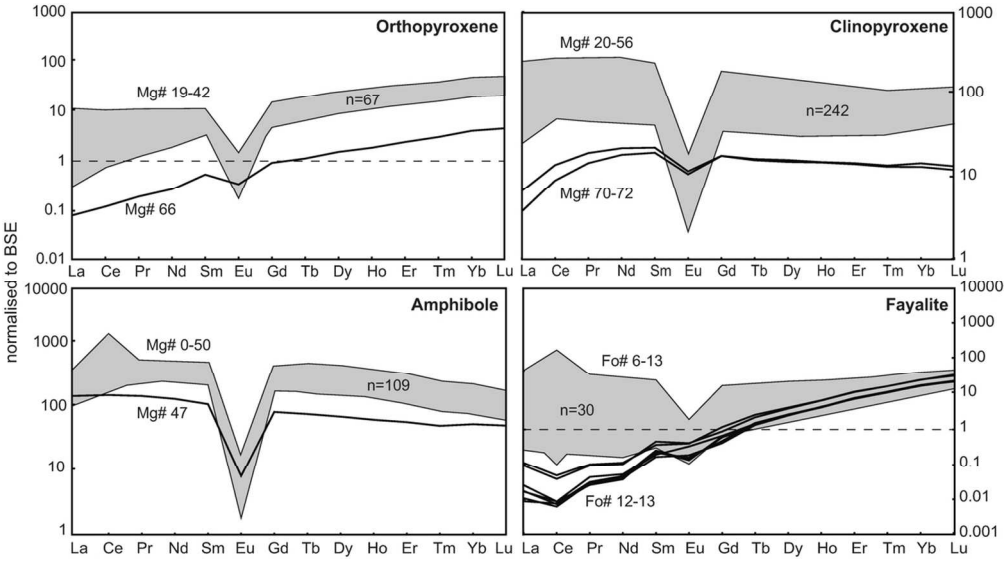

Fig. 8: REE contents in mafic minerals normalised to BSE composition (McDonough & Sun, 1995). Dark grey fields show REE patterns of the majority of crystals, likely to have grown in a highly evolved rhyolitic melt. Black lines indicate REE contents of crystals deviating from the main trend. Crystals depleted in LREE and lacking characteristic Eu anomaly crystallised in less evolved magma prior to significant plagioclase fractionation.

Fig. 8

114x63mm (300 x 300 DPI)

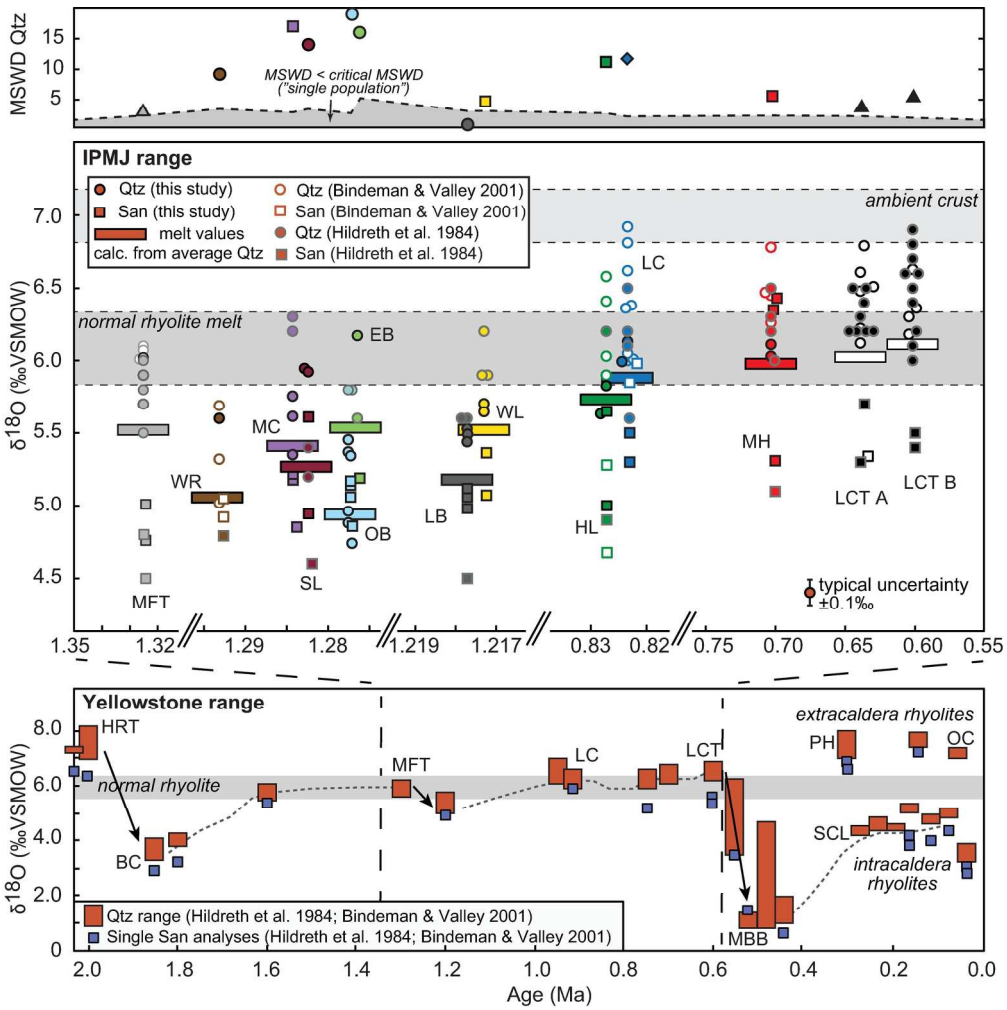

Fig. 9: Oxygen isotopes $\delta^{18}O$ in ‰ VSMOW for explosive end members MFT and LCT and effusive domes and lavas in-between (abbreviations and colours as in Fig. 1). Wide boxes indicate probable $\delta^{18}O_{melt}$ values calculated from average quartz compositions for each unit. Grey background bar illustrates range of "normal"-$\delta^{18}O$ rhyolites (expected values by fractionation of MOR and arc basalts, Bindeman (2008) and references therein). Upper panel defines the MSWD of the quartz analyses. MSWD > $MSWD_{critical}$ indicates that the results do not represent a single population. Lower panel represents trends in $\delta^{18}O$ throughout the history of the Yellowstone volcanic field (after Bindeman and Valley, 2001; Hildreth et al. 1984).

Fig. 9
188x188mm (300 x 300 DPI)

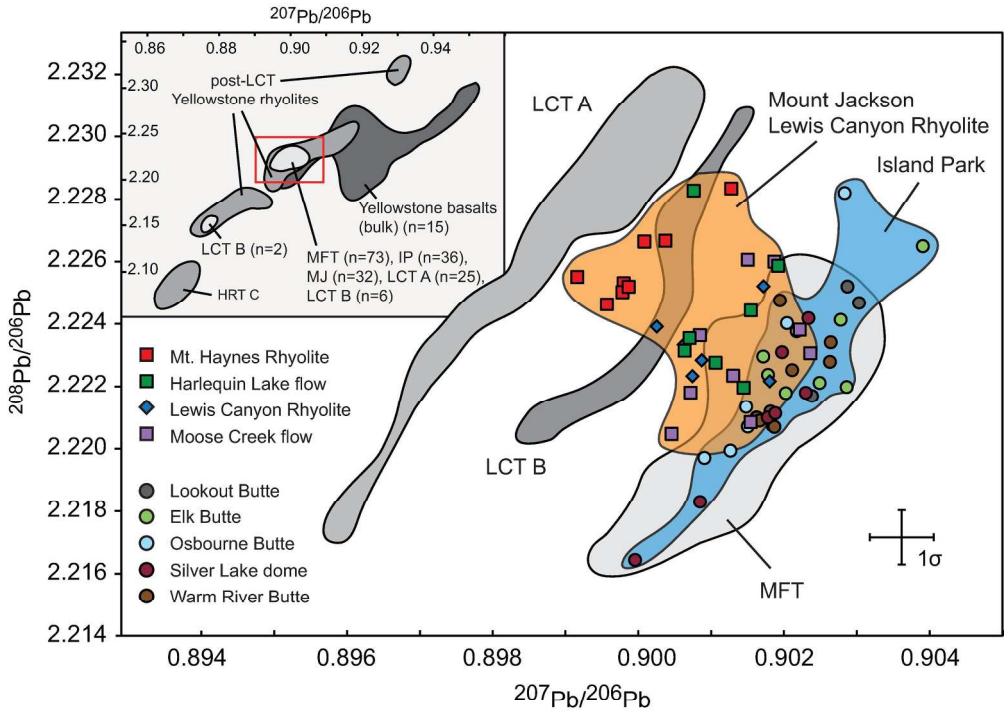

Fig. 10: Pb isotopes in sanidine in IPMJ rhyolites. Inlet diagram shows the entire range of Pb isotopic compositions for the entire Yellowstone volcanic field with red-framed box showing the extent of main diagram. Data for IPMJ rhyolites from this study, MFT from Ellis et al. (unpublished data), other Yellowstone rhyolites and basalts from Doe et al. (1982); Watts et al. (2012).

Fig. 10
212x253mm (300 x 300 DPI)

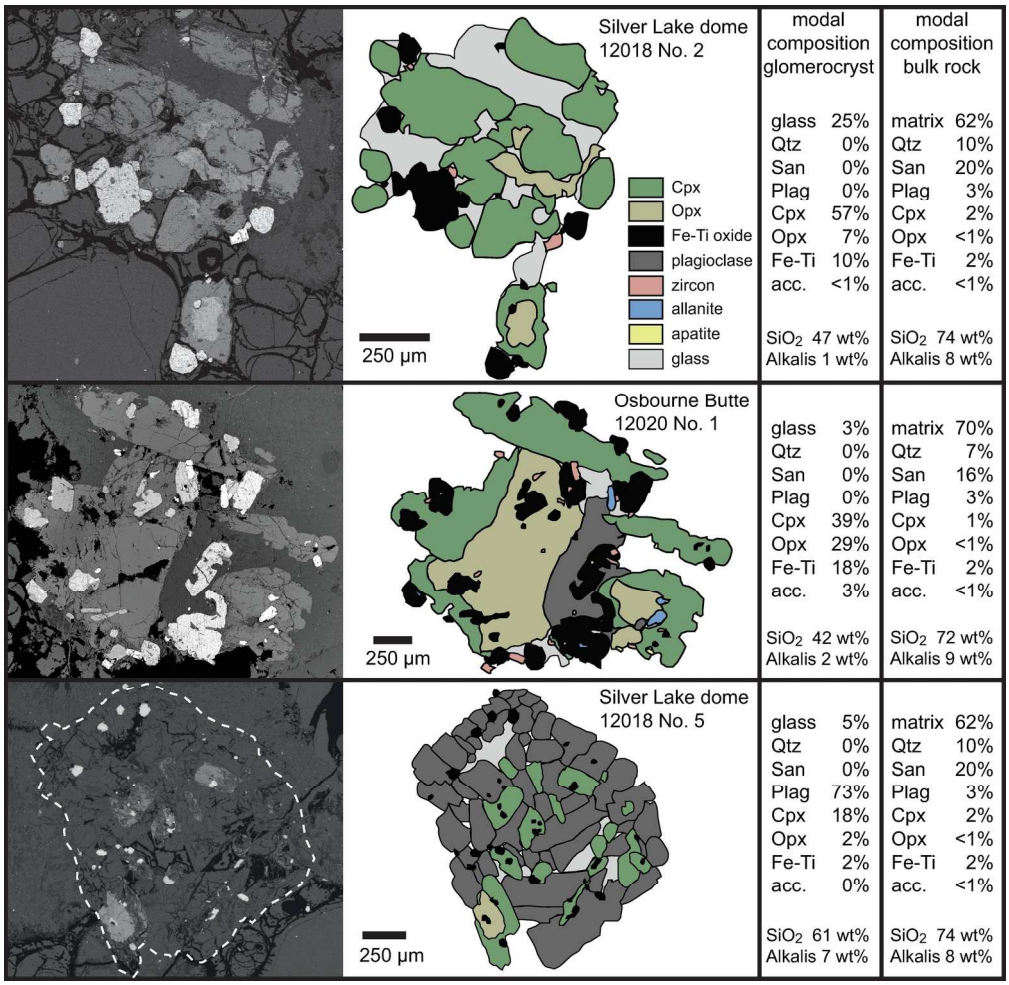

Fig. 11: Example of glomerocrysts from different Island Park domes. Comparison of mineral assemblage within the aggregate with free single crystals yields no significant compositional differences. Bulk glomerocryst compositions are less evolved compared to typical whole rock modal compositions due to the lack of late-forming sanidine and quartz.

Fig. 11
177x173mm (300 x 300 DPI)

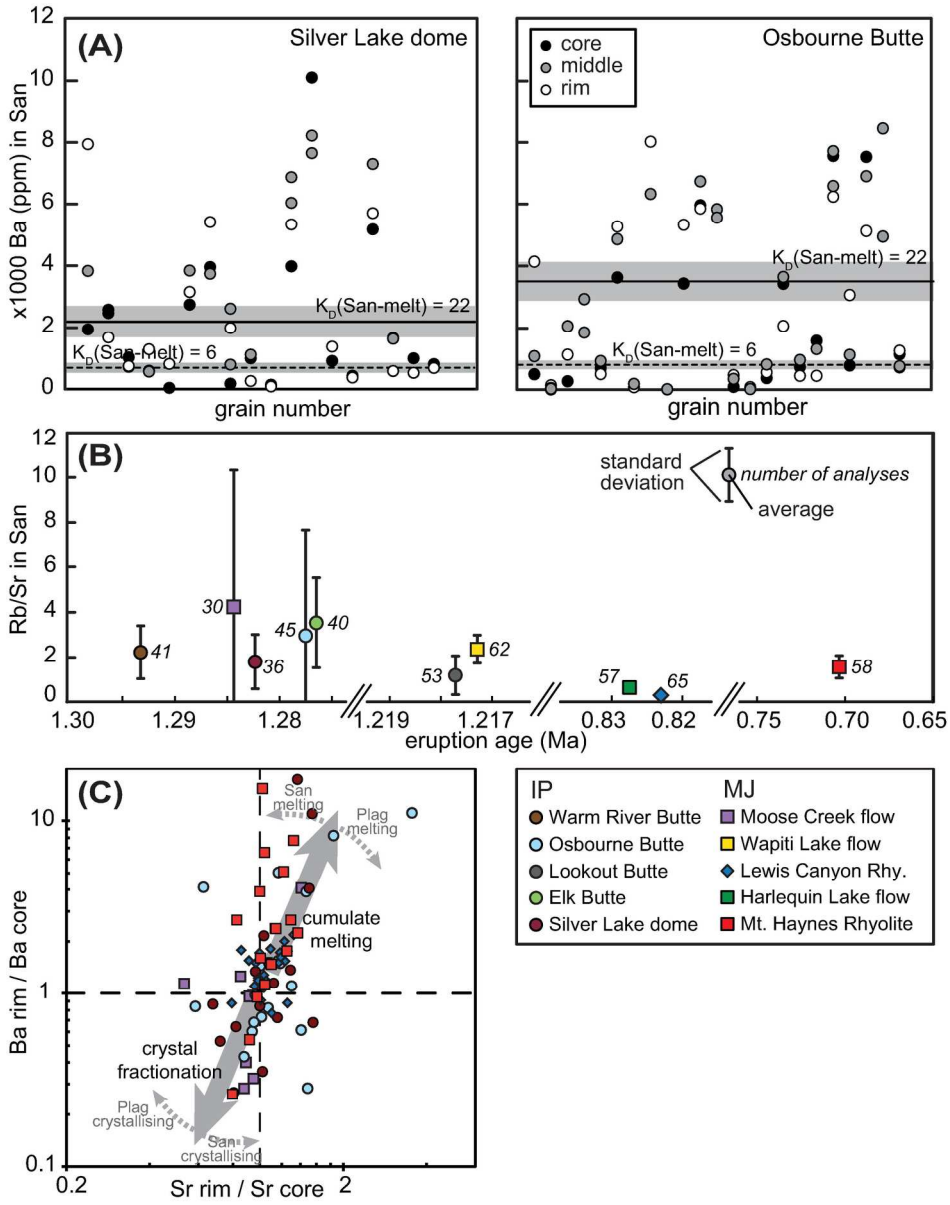

Fig. 12: (A) Ba contents in sanidine rims and cores do not fall into the calculated equilibrium range expected from Ba contents in glass from the same unit. Equilibrium range calculated with K_D(San-melt)≈22 in rhyolite from Leeman and Phelps (1981) and K_D(San-melt)≈6.7 in high-silica rhyolite (Mahood & Hildreth, 1983). Figure contains only data for those sanidine crystals that were imaged via CL. (B) Average Rb/Sr in San for each unit with error bars indicating one standard deviation. Numbers in italic correspond to number of analyses per unit. Note the large variability for IP domes and Moose Creek (MC) compared to MJ flows, indicating higher entrainment component for units close to MFT-related caldera. (C) Ba ratio between rim and core and Sr ratio respectively suggest that reverse zoning in San is due to cumulate remelting or crystallisation from less evolved rhyolite melt. Figure contains only data for those sanidine crystals that were imaged via CL.

Fig. 12
174x222mm (300 x 300 DPI)

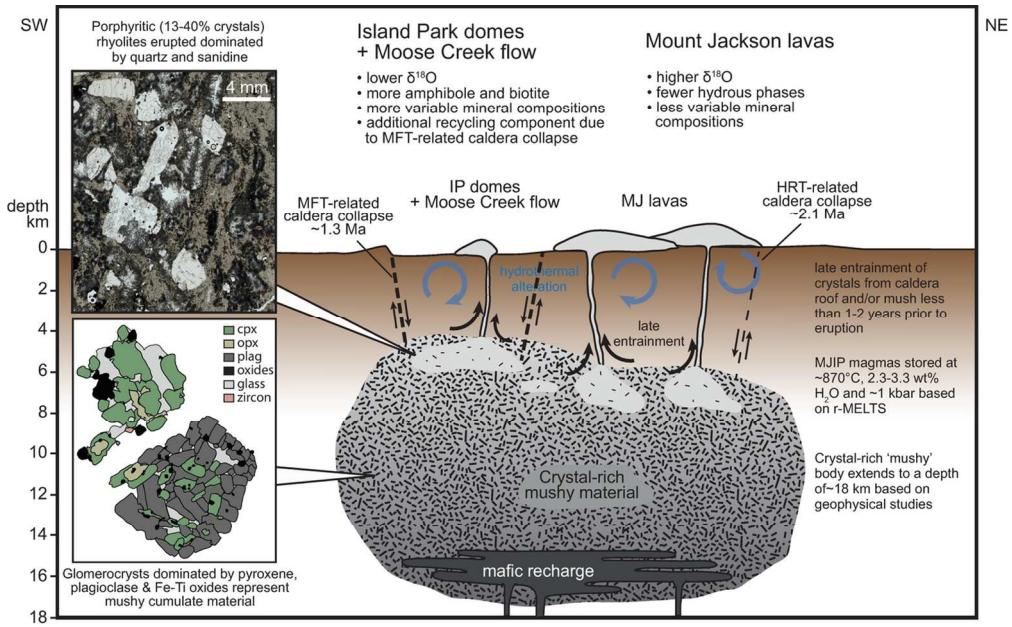

Fig. 13: Schematic summary diagram of petrogenetic processes and characteristics of the IPMJ rhyolite series.
Fig. 13
124x77mm (300 x 300 DPI)

Table 1: Modal mineral abundances in percent determined via point counting on thin sections

Unit	WR	MC	SL	OB	EC	LB	WL	HL	LC	MH
devitrified	D	D	P	P	P	D	P	D	D	D
matrix	70.7	69.4	61.2	60.9	71.8	67.4	86.5	81.6	82.2	81.1
quartz	11.8	16.6	8.2	8.0	7.1	11.3	4.1	9.1	3.9	5.8
sanidine	11.4	8.8	25.5	19.8	16.3	14.8	7.0	5.5	5.9	10.1
plagioclase	3.9	3.2	2.5	7.2	4.3	4.5	1.8	3.1	7.1	2.5
Fe-Ti oxides	1.2	1.0	1.1	1.6	0.3	1.3	0.5	0.6	0.4	0.3
mafic minerals*	1.0	0.9	1.4	2.5	0.3	0.8	0.1	0.1	0.6	0.3
accessories	<0.1	<0.1	<0.1	<0.1	<0.1	<0.1	<0.1	<0.1	<0.1	<0.1

D = fully devitrified, P = partially devitrified, still contains glass shards

Mafic minerals*										
clinopyroxene	0	20.3	61.8	73.6	22.5	34	0	0	67.1	93.3
orthopyroxene	28.6	28.4	15.4	24.2	10	18.4	100	100	25	6.7
fayalite	66.7	16.2	19.5	0	62.5	27.2	0	0	7.9	0
Fe-hornblende	4.8	35.1	3.3	2.2	5	20.4	0	0	0	0

* Due to the scarcity of mafic minerals in thin section mineral abundances of different mafic mineral groups were estimated by number of grains picked after density separation

Table 2: Bulk compositions of IPMJ lavas via XRF and ICP MS

Unit	Warm River Butte	Silver Lake dome	Os-bourne Butte	Elk Creek Butte	Look-out Butte	Moose Creek flow	Wapiti Lake flow	Lewis Canyon Rhy.	Harle-quin Lake	Mt. Haynes flow
series	**IP**	**IP**	**IP**	**IP**	**IP**	**MJ**	**MJ**	**MJ**	**MJ**	**MJ**
sample #	BE SRP 12 027	BE SRP 12 018	BE SRP 12 022	BE SRP 12 024	BE SRP 12 025	BE SRP 12 001	JT 13 019	BE SRP 12 043	BE SRP 12 032	BE SRP 12 036
Major elements via XRF, normalised to 100% anhydrous (wt %)										
SiO_2	76.11	75.54	73.97	78.43	73.54	77.73	77.77	75.74	76.28	77.65
TiO_2	0.17	0.20	0.22	0.11	0.24	0.13	0.12	0.22	0.21	0.14
Al_2O_3	13.29	13.08	13.70	11.69	13.71	12.09	12.04	12.66	12.40	12.02
FeO*	1.76	2.01	2.00	1.19	2.19	1.30	1.15	2.00	1.73	1.31
MnO	0.05	0.04	0.04	0.02	0.03	0.03	0.01	0.03	0.02	0.02
MgO	0.05	0.08	0.12	0.04	0.07	0.03	0.01	0.04	0.12	0.05
CaO	0.46	0.71	0.95	0.48	0.79	0.43	0.36	0.61	0.53	0.32
Na_2O	3.13	3.28	3.51	3.15	3.63	3.26	3.24	3.61	3.40	3.23
K_2O	4.95	5.04	5.45	4.85	5.65	4.97	5.30	5.06	5.28	5.24
P_2O_5	0.02	0.03	0.03	0.04	0.14	0.02	0.01	0.03	0.02	0.01
Trace elements via LA-ICP MS (ppm)										
La	88	85	96	71	83	75	61	56	79	53
Ce	163	156	172	141	139	138	109	130	152	93
Pr	19	17	20	14	16	15	12	12	16	10
Nd	64	60	67	49	55	49	41	43	58	33
Sm	13	12	13	10	10	10	8	9	12	7
Eu	0.9	1.3	1.6	0.5	1.9	0.5	0.4	1.6	1.1	0.4
Gd	10.6	10.1	11.6	9.7	8.7	9.0	8.0	8.0	10.6	6.2
Tb	1.9	1.8	2.0	1.8	1.4	1.7	1.5	1.5	1.9	1.2
Dy	11.3	10.6	11.9	11.5	8.6	10.3	9.8	9.7	11.8	7.6
Ho	2.2	2.1	2.4	2.3	1.7	2.1	2.1	2.0	2.4	1.6
Er	5.6	5.6	6.4	6.5	4.6	5.6	5.7	5.5	6.5	4.5
Tm	0.9	0.8	0.9	1.0	0.7	0.8	0.9	0.8	1.0	0.7
Yb	5.4	5.1	5.7	6.3	4.4	5.3	5.4	5.2	5.9	4.8
Lu	0.8	0.8	0.9	0.9	0.7	0.8	0.8	0.8	0.9	0.7
Ba	420	622	789	207	1098	180	141	901	575	160
Th	34	30	29	31	28	33	35	26	29	31
Nb	49	44	42	43	42	48	50	46	50	52
Y	48	53	60	55	44	50	53	50	62	35
Hf	8.5	8.7	9.1	6.4	9.9	7.0	7.3	10.0	9.3	7.2
Ta	3.7	3.2	3.0	3.5	2.9	3.8	4.0	3.2	3.5	4.0
U	5.7	5.0	5.3	7.1	4.6	7.5	7.6	5.1	6.1	7.3
Pb	32	28	30	30	26	33	25	28	26	29
Rb	121	147	162	175	141	182	230	166	187	223
Cs	2.0	2.3	2.7	3.2	1.7	3.6	2.5	1.8	2.6	2.8
Sr	25	37	48	16	61	13	10	53	29	8
Sc	3.2	3.3	3.5	1.7	3.5	1.7	1.8	3.0	2.3	1.8
Zr	254	277	303	164	350	181	192	345	290	188
Zr sat. T(°C)[1]	843	843	843	795	856	804	807	858	842	806
Zr sat. T(°C)[2]	814±17	810±19	806±21	753±17	820±22	763±18	766±18	824±21	805±20	766±18

[1]Hanchar & Watson (2003); [2]Boehnke et al. (2013)

Table 3: $^{40}Ar/^{39}Ar$ eruption ages

Unit	Abbr.	Series	$^{40}Ar/^{39}Ar$ age (Ma)	analytical uncertainty 2 sig	Full external precision 2 sig	MSWD	non-eruption age grains $n_{non\text{-}eruptive}$ / n_{total}
Warm River Butte	WR	IP	1.2943	0.0020	0.0026	1.44	7 / 30
Moose Creek flow	MC	MJ	1.2856	0.0064	0.0066	0.57	0 / 16
Silver Lake dome	SL	IP	1.2839	0.0112	0.0114	0.88	0 / 28
Osbourne Butte	OB	IP	1.2784	0.0052	0.0054	1.12	1 / 27
Elk Creek Butte	EC	IP	1.2777	0.0090	0.0092	1.01	0 / 29
Lookout Butte	LB	IP	1.2190	0.0144	0.0146	0.9	9 / 19
Wapiti Lake flow	WL	MJ	1.2187	0.0158	0.0160	0.3	0 / 31
Harlequin Lake flow	HL	MJ	0.8300	0.0072	0.0074	1.09	3 / 29
Lewis Canyon Rhyolite	LC	MJ	0.8263	0.0184	0.0186	0.58	10 / 27
Mount Haynes Rhyolite	MH	MJ	0.7016	0.0014	0.0016	1.04	3 / 29